From Diffusion MRI to Brain Connectomics

Aurobrata Ghosh, Rachid Deriche

My chapter

Contents

Chapter 1
From Diffusion MRI to Brain Connectomics

Aurobrata Ghosh and Rachid Deriche

1. commentaire # 1
2. commentaire # 2
3. ...

Abstract Diffusion MRI (dMRI) is a unique modality of MRI which allows one to indirectly examine the microstructure and integrity of the cerebral white matter *in vivo* and *non-invasively*. Its success lies in its capacity to reconstruct the axonal connectivity of the neurons, albeit at a coarser resolution, without having to operate on the patient, which can cause radical alterations to the patient's cognition. Thus dMRI is beginning to assume a central role in studying and diagnosing important pathologies of the cerebral white matter, such as Alzheimer's and Parkinson's diseases, as well as in studying its physical structure in vivo. In this chapter we present an overview of the mathematical tools that form the framework of dMRI – from modelling the MRI signal and measuring diffusion properties, to reconstructing the axonal connectivity of the cerebral white matter, i.e., from Diffusion Weighted Images (DWIs) to the human connectome.

1.1 Introduction

The main objective of this chapter is to present some mathematical models and computational tools for analyzing and modeling the complex central nervous system's (brain and spinal cord) neural connectivity. These models and tools will help to better understand the white matter architecture of the human *central nervous system* (CNS) and in a long term, will also help in addressing important and challenging clinical and neuroscience questions. Indeed, due to our aging society, diseases like Alzheimer's, Parkinson's disease (PD) and depression will affect a large population. These examples of CNS diseases as well as others, like multiple sclerosis have characteristic abnormalities in the microstructure of brain's tissues such as its white matter, which are not apparent and cannot be revealed reliably by standard imaging techniques. Diffusion Magnetic Resonance Imaging (dMRI), a recent imaging modality based on the measurement of the random thermal movement (diffusion) of water molecules within samples, can make visible these co-lateral damages to the fibers of the CNS white matter that connect different brain regions. This is why in this chapter, dMRI is the major anatomical imaging modality that will be considered to recover the neural connectivity in the CNS.

We begin this chapter by presenting the CNS, in particular the brain, before delving into the mathematical framework for dMRI. Section 1.1 is dedicated to a perusal of its general structure and organization, the tissues constituting it, and in highlight, the brain's major neuronal pathways interconnecting its various regions. It aims to provide a context for understanding the general physical problem dMRI attempts to solve.

Aurobrata Ghosh
Athena project-team, INRIA Sophia Antipolis Méditerranée, e-mail: aurobrata.ghosh@inria.fr

Rachid Deriche
Athena project-team, INRIA Sophia Antipolis Méditerranée, e-mail: rachid.deriche@inria.fr

1.1.1 The Central Nervous System

The human nervous system can be divided into the CNS, which consists of the brain and spinal cord and the *peripheral nervous system* (PNS) which consists of the cranial and spinal nerves and their ganglia.

The CNS is the largest part of the nervous system and is composed of the spinal cord and the brain which comprises a lower part, the brainstem, and an upper part, the prosencephalon or forebrain composed of two main units. One is known as the diencephalon. It is located in the midline of the brain and contains the thalamus and the hypothalamus. The other is called the telencephalon or cerebrum and holds the lateral ventricles, the basal ganglia and the cerebral cortex. The brainstem is also composed of two units: the mesencephalon or midbrain and the rhombencephalon or hindbrain which connects the forebrain and midbrain to the spinal cord.

The nervous system is made of about 100 billion nerve cells, or neurons, able to generate and propagate electrical signals to process and transmit neural information. Neurons can receive electrical stimulation from other neurons on their soma, through their multiple dentrites. They can integrate this information and propagate it to more or less distant locations of the cerebrum by an extension called an axon. Nerve signal communication is performed at specialized loci called synapses. Each neuron has on average 1000 synaptic connections with other neurons. This yields about 100 trillion connections within a human brain. All these synapses result in an impressively dense and complex network between functional areas, which can be understood as aggregates of nerve cells' soma and dendrites. They are essentially located in the grey matter while the underlying wiring constitutes the white matter. According to the connectionist point of view, the human brain is organized into distinct processing regions interconnected by a network of anatomical relays. Processing units handle the execution of primary cognitive functions, and higher cognitive tasks arise from a global coordination between these processing units. Neural signal is processed in the cerebral cortex and transmitted to various regions of the brain through the white matter. So we distinguish:

- The *grey matter* essentially forms the outer part of the cerebrum, some nuclei within the brain, as well as the deeper part of the spinal cord. It is made of neurons and their unmyelinated fibers. The cerebral cortex is the most important structure of the grey matter and plays a major role in various functions such as memory, attention and language.
- *White matter* is composed of axonal nerve fibers, covered by a myelin sheath giving its distinctive colour in MRI. It is found in the inner layer of the cortex, the optic nerves, the central and lower areas of the brain and surrounding the central shaft of grey matter in the spinal cord.

The CNS white matter axons can be distributed diffusely or concentrated in bundles, also referred to as tracts or fiber pathways. The brain's white matter pathways are generally categorized into commissural, association and projection fibers, depending on the areas they connect (see Fig. 1.1).

- The *commissural tracts* connect a region in one hemisphere to another region of the opposite hemisphere.
- The *association tracts* connect various cortical areas within a given hemisphere.
- The *projection tracts* connect the cortex to deep brain regions such as the thalamus or the spinal cord.

In the spinal cord, it is the grey matter that is located in the center with a typical H-shaped appearance in transverse sections. It is surrounded by white matter which contains long ascending and descending pathways.

1.1.2 In Vivo CNS Connectivity

Compared to the understanding of neural circuitry in animals as cats or mice where the use of invasive tracers is possible [59], the knowledge of the human brain organization is relatively poor. Therefore, how to study the connectivity information about the CNS anatomy, in particular, about the cerebral and spinal cord white matter? Anatomical MRI allows us to distinguish and classify grey matter and white matter. However, with this contrast, white matter retains a homogeneous aspect, preventing any observation of neural fibers and thus of neuronal connectivity. Cerebral and spinal dissection used to be the only means of accessing the neural architecture [22, 30, 74]. Then, anatomists started using chemical markers to do neuronography [55, 59]. More recently, neural fiber tractography based on local injection of

chemical markers and subsequent observation of the induced propagation yielded high-quality connectivity mapping in the cat and monkey cerebral cortices [75, 59].

The relatively recent development of dMRI, which uses the orientational preference of water molecules in diffusing along the directions of the fibers has brought in the last twenty years great hopes for the non-invasive exploration of the neural anatomy of the CNS. Indeed dMRI provides a non-invasive way of estimating in vivo CNS fiber structures using the average random thermal movement (diffusion) of water molecules as a probe. Diffusion MRI is a field of research with a history of roughly three decades. It was introduced in the mid 80's by Le Bihan et al. [39], Merboldt et al. [43] and Taylor et al. [63]. As of today, it is the unique non-invasive technique capable of describing the neural connectivity in vivo by quantifying the anisotropic diffusion of water molecules in biological tissues. The great success of dMRI comes from its ability to accurately describe the geometry of the underlying microstructure and to probe the structure of the biological tissue at scales much smaller than the imaging resolution.

The diffusion of water molecules is Gaussian in an isotropic medium and under normal unhindered conditions, but in fibrous structure such as white matter, the diffusion is very often directionally biased or anisotropic and water molecules tend to diffuse along fibers. For example, a molecule inside the axon of a neuron has a low probability to cross a myelin membrane. Therefore the molecule will move principally along the axis of the neural fiber. Conversely if we know that molecules diffuse locally principally in one direction, we can infer that this corresponds to a set of fibers.

1.1.3 Organization of the Chapter:

Section 1.2 briefly covers the historical development of Nuclear Magnetic Resonance (NMR) and MRI to set the stage. We explore the physics of the signal generation in NMR and how diffusion properties can be measured non-invasively from NMR in Sect. 1.3. Section 1.3 begins by presenting the fundamental ideas of NMR. Section 1.3.1 then presents the crucial spin echo experiment proposed by Hahn, which is a corner stone experiment that led to the development of diffusion NMR. Next in Sect. 1.3.2 we describe diffusion in considerable detail. Section 1.3.3 then presents the pulse-field-spin-echo (PGSE) experiment that was proposed by Stejskal and Tanner. This important experiment is the modern and practical approach for measuring diffusion from NMR. The Stejskal-Tanner model for the diffusion NMR signal is based on Fick's laws of diffusion. Section 1.3.4 presents next the q-space approach for modelling the diffusion NMR signal, which is based on Einstein's random walk approach to Brownian motion.

Section 1.4 is dedicated to dMRI reconstruction algorithms that allow to go beyond simply measuring intrinsic diffusion properties from NMR/MRI to inferring the microstructure of the underlying tissue non-invasively. Section 1.4.1 presents diffusion tensor imaging (DTI), the most widely used dMRI algorithm with the simplest experimental requirements, but with powerful applications. DTI is however limited under certain microstructure configurations. Section 1.4.2.1 presents diffusion spectrum imaging (DSI), which allows to overcome these limitations. Finally Sect. 1.4.2.2 presents Q-Ball imaging, which can recover complex microstructures like DSI, but isn't limited by the latter's lengthy acquisition schemes.

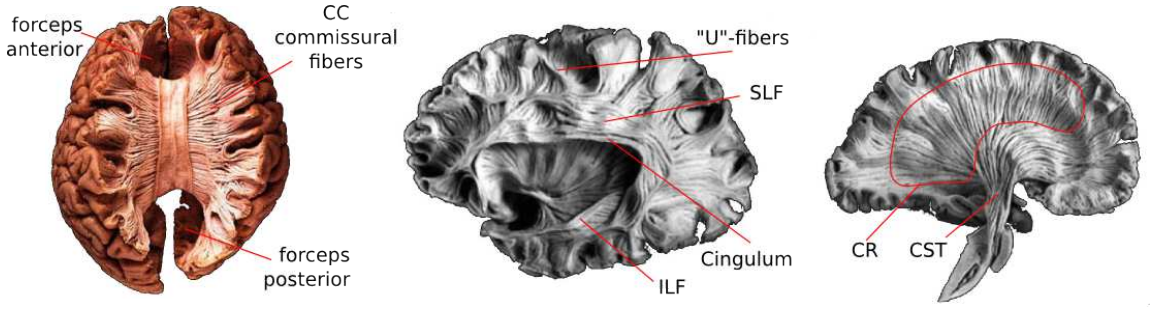

Fig. 1.1 Major white matter fiber pathways in the brain. (a) Commissural tracts – the Corpus Callosum (CC). (b) Association tracts – short "U"-fibers connecting neighbouring gyri, the Superior Longitudinal Fasciculus (SLF), the Cingulum and the Inferior Longitudinal Fasciculus (ILF). (c) Projection tracts – the Corona Radiata (CR) and the Corticospinal Tract (CST). Adapted from [74].

Section 1.5 introduces briefly the computational framework consisting of sophisticated mathematical tools that have been developed for processing dMRI data and images, since these represent complex mathematical objects. In particular we present various metrics for a field of diffusion tensors in Sect. 1.5.1, an algorithm that ensures that the estimated diffusion tensors are in the proper space of symmetric positive definite matrices using a Riemannian metric in Sect. 1.5.2, and a segmentation algorithm for segmenting fields or images of diffusion tensors in Sect. 1.5.3.

Section 1.6 is dedicated to tractography – algorithms that integrate local microstructure information to reconstruct white matter fiber pathways. Section 1.6.1 presents deterministic approaches while Sect. 1.6.2 presents probabilistic approaches. The penultimate section – Sect. 1.7, is dedicated to applications. It presents the impacts of dMRI in both clinical and neuroscientific scenarios, and highlights its usefulness.

The chapter concludes with a summary in Sect. 1.8. In Sect. 1.9 we provide an incomplete list of important internet resources in terms of available softwares and database for processing dMRI data.

1.2 A Brief History of NMR and MRI

The scientific heritage of NMR and MRI is reflected in the list of Nobel laureates who contributed to their developments. The theoretical underpinnings that made NMR possible were proposed in 1924 by Wolfgang Pauli who suggested a new quantum degree of freedom that later came to be known as spin. He formulated the mathematical theory by 1927, and was awarded the Nobel prize in physics in 1945 for his contributions. The concept of spin implies that atomic nuclei bearing spins exhibit magnetic moments. The fact that protons exhibit magnetic moments had already been discovered in 1922 by Otto Stern prior to the concept of spin. Stern was awarded the Nobel prize in physics in 1943. Pauli's theory was verified in 1938 by Isidor Rabi in molecular beams. From his experiments Rabi was able to both detect the effects of spin and measure the gyromagnetic ratio that is the characteristic signature of an atomic nucleus due to its spin. His experiments also established the concept and the technique of NMR for manipulating spins. Rabi was awarded the Nobel prize in physics in 1944.

In 1946 Felix Bloch [12] and Edward Mills Purcell [56] independently extended the techniques established by Rabi. They successfully demonstrated the magnetic resonance effect in liquids and solids. Bloch and Purcell shared the Nobel prize of 1952 in physics, and NMR was established. In his seminal paper of 1950 [31] Erwin Hahn proposed the spin echo experiment, which used a combination of 90^o and 180^o electromagnetic or radio frequency pulses to filter out effects of magnetic field inhomogeneities in the measurement of the transverse signal. Further works of Herman Carr and Purcell in 1954 [14] led to the full development of the radio frequency pulse technique introduced by Hahn. This formed the foundations of NMR.

It must be noted at this point that both the papers of Hahn [31] and Carr & Purcell [14] critically point out the observed effects of diffusion of the spin bearing nuclei in magnetic resonance experiments with a succession of radio frequency pulses. Although these papers generally perceive the diffusion effect as an unfortunate phenomenon resulting in a loss of signal, Carr & Purcell [14] in fact demonstrate that diffusion can be directly measured from NMR and go on to actually measure the diffusion constant of water at 25^oC. This forms the corner-stone of diffusion NMR.

Although NMR became a well established technique for studying various materials, it took almost three decades since the experiments of Bloch and Purcell in 1946, for MRI to be invented. NMR by itself is capable of examining a single spin ensemble or a tiny region of a sample, but it can't image the whole sample to recreate a 2D slice or a 3D volumetric image necessary to study entire biological samples like the human body. Paul Lauterbur in 1973 [37] proposed the use of magnetic gradient fields to spatially encode the positions or voxel regions of the spin ensembles. This was a remarkable invention, which made it possible to reconstruct entire slice or volumetric images from NMR data. Spatial encoding was improved in terms of frequency encoding by Richard Ernst in 1978, and phase encoding by Bill Edelstein in 1980 using pulsed gradients. In 1977 Peter Mansfield [42] developed the mathematical framework for rapidly switching gradients for spatial encoding, greatly speeding up the process of reconstructing images of an entire biological sample. This is known as *echo planar imaging* (EPI). Lauterbur and Mansfield were jointly awarded the Nobel prize in medicine in 2003 for making MRI possible. Thus modern MRI was developed from the phenomenon of NMR coupled with the method of spatial encoding.

1.3 Nuclear Magnetic Resonance & Diffusion

The principles of NMR are based on *spin*, a fundamental quantum characteristic possessed by electrons, protons, and neutrons, like electrical charge and mass. Spins come in multiples of 1/2 and can be positive or negative. In grouped particles, e.g. atomic nuclei, opposite spin-signs can pair up to eliminate the total spin of the group. But the net spin of unpaired particles or atomic nuclei imparts a magnetic dipole moment. In other words such particles or such atomic nuclei can be influenced by an external magnetic field. In the presence of a strong magnetic field $\mathbf{B_0}$ with magnitude B_0, the magnetic dipole moment vector or the spin vector of the particle or nucleus aligns itself with $\mathbf{B_0}$ and precesses around it with an angular frequency known as the *Larmor frequency* $\omega_0 = \gamma B_0$, where γ is the *gyromagnetic ratio*, characteristic of the particle or the nucleus. The effect is detectable when it becomes pronounced in the presence of an ample collection of spin bearing particles or nuclei with the same gyromagnetic ratio. From a macroscopic perspective, when such a collection is subjected to a magnetic field, the randomly oriented individual magnetic dipole moment vectors align themselves along $\mathbf{B_0}$. Laws of thermodynamics ensure that a greater number of spins point along the magnetic field (low energy configuration) than opposite to it (high energy configuration). This forms a resultant ensemble magnetic dipole moment vector $\mathbf{M}$. Conventionally the external magnetic field $\mathbf{B_0}$ is considered to be aligned with the Z-axis. The XY-plane is then known as the transverse plane, and the net magnetization vector $\mathbf{M}$ can be separated into the *longitudinal* component $\mathbf{M}_z$, along the Z-axis (or $\mathbf{B_0}$), and the *transverse* component $\mathbf{M}_{xy}$, in the transverse plane (Fig. 1.2).

Of particular interest is the hydrogen nucleus ^1H, which is found abundantly in nature, accounting for 99.98% of all hydrogen atoms, and also constituting water. 60% of the human body and 78% of the brain is water. Therefore, ^1H is a natural spin bearing nucleus of choice for MRI. ^1H is an unpaired proton with a net spin of 1/2, and has a gyromagnetic ratio of $\gamma = 42.58$ MHz/T.

The NMR signal is generated by exposing the ensemble of spins precessing along $\mathbf{B_0}$ to an oscillating magnetic field or an electro-magnetic (radio-frequency: RF) pulse. This is known as the excitation phase. The energy absorbed by the low energy configuration spins from this pulse tilts the magnetization vector $\mathbf{M}$ away from $\mathbf{B_0}$ towards the high energy configuration. The oscillation of the secondary magnetic field ensures that the spins (and hence $\mathbf{M}$) continue to precess around $\mathbf{B_0}$ even tilted away from it – along the surface of a cone (Fig. 1.2). Once the RF pulse is switched off, the spins begin to recover their alignment with the main magnetic field $\mathbf{B_0}$, and to return to their low energy configuration or the thermal equilibrium. This is known as the relaxation phase. The signal is created as the spins precess tilted away from $\mathbf{B_0}$, and it decays as the spins relax, dissipating the absorbed energy. The longitudinal relaxation and the transverse relaxation of $\mathbf{M}$ are governed by different phenomena and are characterized by different time signatures.

The *longitudinal relaxation* is known as the T1 relaxation since it is described using a time signature denoted T1. The T1 relaxation occurs as the spin ensemble radiates the energy it had absorbed from the RF pulse to the surrounding thermal reservoir or lattice and regains its thermal equilibrium with the lattice. Therefore, the T1 relaxation is also known as the *spin-lattice* relaxation. In this process the

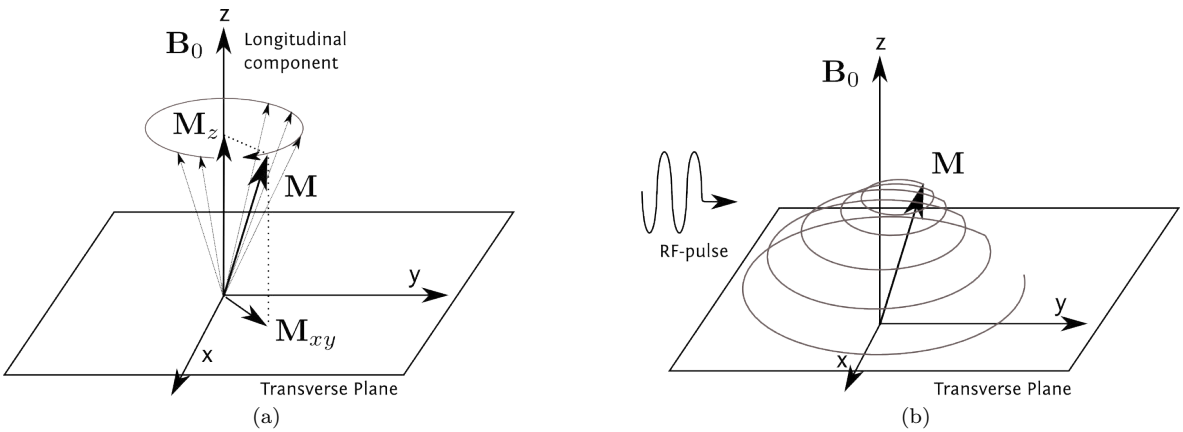

Fig. 1.2 Nuclear Magnetic Resonance. (a) A net magnetization dipole moment vector $\mathbf{M}$ forms when spins are exposed to an external magnetic field $\mathbf{B_0}$. (b) The NMR signal is generated by exciting the ensemble of spins precessing along $\mathbf{B_0}$ by exposing them to a radio-frequency pulse – the magnetization vector $\mathbf{M}$ spirals down to the transverse plane in the fixed frame of reference.

spins realign themselves with $\mathbf{B_0}$. In terms of the net magnetization vector $\mathbf{M}$, this implies that the longitudinal component $\mathbf{M}_z$ progressively regains its initial magnitude, while the transverse component $\mathbf{M}_{xy}$ progressively becomes null again.

The *transverse relaxation* involves the phenomenon of the spins regaining their thermal equilibrium amongst themselves, and is characterized by the time signature T2. Therefore it is also known as the *spin-spin* relaxation or the T2 relaxation. In the transverse plane this is interpreted by the spins losing their initial coherence. From an initial coherent transverse magnetization vector $\mathbf{M}_{xy}$, they progressively dephase as they radiate the energy they had absorbed to neighbouring spins. Transverse relaxation is, however, a complex phenomenon. Although theoretically $\mathbf{B_0}$ is supposed homogeneous, in reality minor inhomogeneities exist. These inhomogeneities are relevant enough to also contribute to spins dephasing in the transverse plane, though this is not a true relaxation. Transverse relaxation is therefore a combination of spin-spin relaxation and field inhomogeneity dephasing. The pure spin-spin relaxation time is known as T2. The combined transverse relaxation time is known as T2*.

The *Bloch equations* are a coupled set of three differential equations that combine the effects of NMR and describe the evolution of the net magnetization vector $\mathbf{M}$ over time. These are macroscopic and phenomenological equations that include the effects of Larmor precession and T1 and T2 relaxations. They are written in the fixed frame of reference in terms of the relaxation time constants as:

$$\frac{d\mathbf{M}(t)}{dt} = \gamma \mathbf{M}(t) \times \mathbf{B}(t) + \begin{pmatrix} -\frac{1}{T_2} & 0 & 0 \\ 0 & -\frac{1}{T_2} & 0 \\ 0 & 0 & -\frac{1}{T_1} \end{pmatrix} \mathbf{M}(t) + \begin{pmatrix} 0 \\ 0 \\ \frac{M_0}{T_1} \end{pmatrix}, \tag{1.1}$$

where $\mathbf{B}(t)$ is the total external magnetic field.

1.3.1 The Hahn Spin Echo Experiment

Erwin L Hahn was the first to notice the effects of diffusion when he conceived the *spin echo* experiment to remove the effects of field inhomogeneities or T2* from the signal [31]. Diffusion NMR is derived from Hahn's original spin echo experiment of 1950. Hahn put forth the idea that following a 90^o RF pulse that tilts the net magnetization vector to the transverse plane, the dephasing that follows caused by the field inhomogeneities, could be refocused using a second RF pulse of 180^o, thus removing the effects of the field inhomogeneities.

After the 90^o RF pulse, the spins precessing in the transverse plane should appear static in a frame of reference rotating at the Larmor frequency. However, due to field inhomogeneities, as the spins begin to

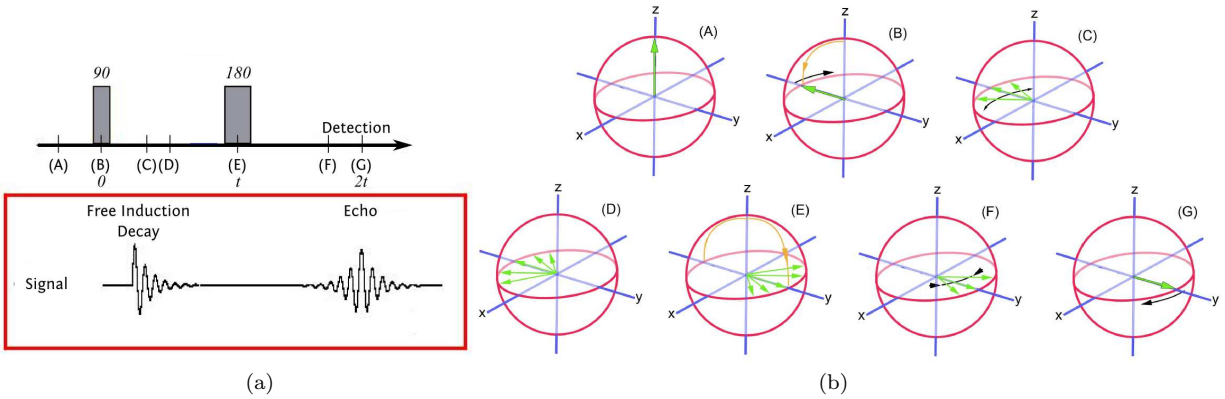

Fig. 1.3 The Hahn Spin Echo experiment. (a) Pulse sequence with Free Induction Decay & signal echo. Adapted from Wikipedia. (b) Concept of spin echo refocussing in the rotating frame of reference. (A) The net magnetization vector $\mathbf{M}$ (green vector), initially aligned with the Z-axis under the influence of $\mathbf{B_0}$. (B) 90^o RF pulse tilts (orange arrow) $\mathbf{M}$ on to the transverse plane. (C) & (D) Spins dephasing due to local field inhomogeneities. Slow spins fall back, while the fast spins move ahead in the transverse plane. (E) 180^o RF pulse (orange arrow) flips the spins around such that now the slow spins are ahead and the fast spins are behind. (F) Refocussing begins as the fast spins begin to catch up the slow spins from behind. The echo begins to form. (G) The spins are completely refocussed. This is the centre of the echo and the signal is free of the effects of field inhomogeneities. Drawing by A.G. Filler, image source Wikipedia.

dephase, some would appear to speed up (or move ahead clockwise in the rotating frame of reference), while some would slow down (or fall back anti-clockwise in the rotating frame of reference). This transverse dephasing is known as the *free induction decay* (FID) and causes the signal to decay faster than pure T2 effects. However the application of a second RF pulse of 180^o has the effect of flipping the individual spins in the transverse plane such that the "slow" spins that had fallen behind the rotating frame of reference are flipped ahead of it, while the "fast" spins that had moved ahead are flipped behind the rotating frame of reference. Indeed, the 180^o RF pulse causes the spins to refocus after a certain length of time as the fast spins catch up with the slow spins, which regenerates the signal. This is known as the *echo* and it is free of the $T2^*$ effects due to field inhomogeneities (Fig. 1.3).

It must be noted, however, that the echo regenerates the signal completely only under the assumption that none of the spins in the ensemble have moved. If they move then the 180^o RF pulse doesn't completely invert the spin and this results again in signal decay. However, this is not due to field inhomogeneities. As noted by Hahn [31] and Carr & Purcell [14], this is due to the translational motion of diffusion. This forms the basis of diffusion NMR.

1.3.2 Diffusion

Diffusion NMR (dNMR) is a modality of NMR that is sensitive to the Brownian motion of the particles in a sample. The dNMR experiment can therefore be used to measure the diffusion properties of the underlying sample. This makes dNMR central to diffusion MRI. At the heart of dNMR is the diffusion process, and understanding diffusion helps to understand how it can be measured from NMR. It leads to the critical improvements that were made by Stejskal & Tanner to the original spin echo experiments of Hahn and Carr & Purcell that opened up the domain of dNMR.

Diffusion is a process of mass transport that describes the random spreading of molecules or particles generally in the presence of a concentration gradient. The process of diffusion was observed, studied and mathematically described over the entire 19th century. It was initially observed in three different forms, namely heat diffusion in the presence of a temperature gradient, molecular diffusion in the presence of a concentration gradient, and Brownian motion, which occurs even in the absence of any gradients. These, apparently very different phenomena – the first, concerning the spreading of energy in a solid medium, the second, concerning the spreading of molecules from a region of high concentration to a region of low concentration in fluids, and the third, concerning the random motion of molecules and particles in fluids due to the ambient temperature – can all be described by the same diffusion equation. However, while today their correspondence is widely accepted, establishing this connection wasn't always an easily demonstrable task.

Fick's Laws of Diffusion: The phenomenological equations of diffusion were proposed by Joseph Fourier in 1822 to describe the diffusion of heat in solids, and then adapted by Adolf Fick in 1855 to describe the diffusion of molecules in fluids in the presence of a concentration gradient [21]. Fick derived his "laws of diffusion" from Fourier's laws by analogy, while attempting to describe the experiments conducted by Thomas Graham in 1831 on the diffusion of gases. These laws describe the molecular transfer or diffusion that takes place in a system from regions of high concentration to regions of low concentration due to the concentration gradient.

Fick's first law relates the rate of transfer of the diffusing substance per unit area, or flux $\mathbf{J}$, to the concentration gradient $\mathbf{C}$ causing the diffusion:

$$\mathbf{J} = -D\nabla\mathbf{C}, \tag{1.2}$$

where D is the diffusion coefficient. Conservation of mass during the diffusion process implies $-\nabla\mathbf{J} = \partial\mathbf{C}/\partial t$. This leads to Fick's second law of diffusion:

$$\frac{\partial\mathbf{C}}{\partial t} = D\nabla^2\mathbf{C}. \tag{1.3}$$

Fick's second law describes the change of the concentration field over time due to the diffusion process. Eq. (1.3), which relates the time derivative of the concentration to the second order spatial derivative of the concentration is known as the *diffusion equation* – it describes diffusion phenomenologically.

D being a scalar quantity in Eqs. (1.2 – 1.3) is an indication that diffusion is equal in all directions. This is known as *isotropic* diffusion. However, certain media such as crystals, textile fibers, etc. can be

inherently anisotropic and can favour diffusion in a certain spatial direction while hindering it in others. This results in *anisotropic* diffusion, which is described by replacing the scalar diffusion coefficient D by a generalized *diffusion tensor* $\mathbf{D}$ (3×3 matrix) in Fick's laws [21]:

$$\mathbf{J} = -\mathbf{D}\nabla\mathbf{C}, \tag{1.4}$$

$$\frac{\partial \mathbf{C}}{\partial t} = \nabla \cdot (\mathbf{D}\nabla\mathbf{C}). \tag{1.5}$$

Diagonalizing the diffusion tensor $\mathbf{D}$ into its eigenvalues and eigenvectors provides a local orthogonal coordinate system that indicates the preferential diffusion direction favoured by the anisotropy of the underlying material. This is the budding idea that indicates that diffusion can be considered as a probe of the underlying medium's microstructure. Isotropic diffusion can be understood as a special case of anisotropic diffusion when $\mathbf{D} = D\mathbf{I}$, where $\mathbf{I}$ is the identity matrix. The idea of the diffusion tensor is central to dMRI, since the fibrous quality of the cerebral white matter also exhibits directional anisotropy.

Brownian Motion & Einstein's Random Walk Approach: Although Fick's laws are concerned with the diffusion of molecules from regions of high concentration to regions of low concentration, they essentially describe the evolution of the concentration gradient over time and space, and aren't concerned with the movements of the molecules themselves. The molecular description of diffusion emerged with Albert Einstein in 1905 when he related the molecular-kinetic theory of heat to the observations made by Robert Brown in 1828. Brown had noted the perpetual erratic motion of pollen grains suspended in water while observing them under a microscope. This erratic movement came to be known by his name as Brownian motion. When Einstein proposed [28] that due to the thermal kinetic energy of molecules, particles suspended in a liquid large enough to be observed under a microscope would exhibit random movements governed by the probabilistic law he derived, his idea was quickly recognized to be the theoretical description of Brownian motion. It turned out that the probabilistic law of Brownian motion derived by Einstein also satisfied the diffusion equation. This provided the final link and showed that diffusion was driven by the thermal kinetic energy of molecules due to the ambient temperature, implying that diffusion, in the form of Brownian motion also occurred in the absence of a temperature or a concentration gradient. The special case of diffusion when the suspended particles belong to the liquid is known as *self diffusion*.

To describe the erratic movement of a large number of particles undergoing Brownian motion, Einstein adopted the probabilistic approach of a random walk model [28]. He modelled diffusion using two Probability Density Functions (PDF)s – $f(\mathbf{x}, t)$, the probability of finding a particle at the position $\mathbf{x}$ at a time t, and $P(\Delta\mathbf{x}, \Delta t)$, the transition probability or the probability of finding a particle at a distance $\Delta\mathbf{x}$ from its initial position after a time Δt. Considering $P(\Delta\mathbf{x}, \Delta t)$ symmetric, such that $P(\Delta\mathbf{x}, \Delta t) = P(-\Delta\mathbf{x}, \Delta t)$, Einstein proposed the relation between $f(\mathbf{x}, t)$ and $P(\Delta\mathbf{x}, \Delta t)$:

$$f(\mathbf{x}, t + \Delta t) = \int_{-\infty}^{\infty} f(\mathbf{x} - \Delta\mathbf{x}, t) P(\Delta\mathbf{x}, \Delta t) d\Delta\mathbf{x}. \tag{1.6}$$

He then showed that $f(\mathbf{x}, t)$, which can also be considered as the local particle concentration, satisfies the diffusion equation:

$$\frac{\partial f(\mathbf{x}, t)}{\partial t} = D\nabla^2 f(\mathbf{x}, t), \tag{1.7}$$

which introduces the diffusion coefficient D, showing that the random walk approach can model diffusion. In the isotropic case discussed by Einstein, he further showed that the diffusion coefficient is directly proportional to the variance of the particle displacement $\left\langle (\Delta x)^2 \right\rangle = 2\Delta t D$, where without loss of generality x is any chosen spatial direction. A similar development in the anisotropic case along the lines proposed by Einstein results in the anisotropic diffusion equation and connects the diffusion tensor to the covariance tensor:

$$\frac{\partial f(\mathbf{x}, t)}{\partial t} = \nabla \cdot (\mathbf{D}\nabla f(\mathbf{x}, t)), \tag{1.8}$$

$$\mathbf{D} := \frac{1}{2\Delta t} \begin{pmatrix} \left\langle (\Delta x)^2 \right\rangle & \langle \Delta x \Delta y \rangle & \langle \Delta x \Delta z \rangle \\ \langle \Delta y \Delta x \rangle & \left\langle (\Delta y)^2 \right\rangle & \langle \Delta y \Delta z \rangle \\ \langle \Delta z \Delta x \rangle & \langle \Delta z \Delta y \rangle & \left\langle (\Delta z)^2 \right\rangle \end{pmatrix}. \tag{1.9}$$

Finally Einstein also derived that under the initial condition $f(\mathbf{x}, 0) = \delta(\mathbf{x})$, which corresponds to free diffusion, the local particle concentration $f(\mathbf{x}, t)$ is a Gaussian function with the derived variance $2tD$.

This, however, implies that the Green's function of the diffusion equation, or the transition probability is also a Gaussian in the case of free diffusion:

$$P(\Delta\mathbf{x}, \Delta t) = \frac{1}{(4\pi\Delta t)^{3/2}|\mathbf{D}|^{1/2}} \exp\left(-\frac{\Delta\mathbf{x}^T\mathbf{D}^{-1}\Delta\mathbf{x}}{4\Delta t}\right). \tag{1.10}$$

In the anisotropic case it is an oriented Gaussian parameterized by the covariance tensor.

1.3.3 The Stejskal-Tanner PGSE Experiment

After Hahn who first noticed the effects of diffusion in NMR in his spin echo experiment [31], Carr & Purcell measured the diffusion coefficient for the first time from NMR. In their modification to Hahn's experiment they employed a temporally constant magnetic gradient field and modelled the diffusion of spin bearing particles with discrete jumps [14]. However, the continuous description was formulated by Torrey in 1956. He modified the phenomenological Bloch equations by adding to it Fick's diffusion equation (Eq. 1.3) [64]. This came to be known as the Bloch-Torrey equation for describing the net magnetization vector $\mathbf{M}$ (without flow):

$$\frac{\partial\mathbf{M}}{\partial t} = \gamma\mathbf{M}\times\mathbf{B} + \begin{pmatrix} -\frac{1}{T_2} & 0 & 0 \\ 0 & -\frac{1}{T_2} & 0 \\ 0 & 0 & -\frac{1}{T_1} \end{pmatrix}\mathbf{M} + \begin{pmatrix} 0 \\ 0 \\ \frac{M_0}{T_1} \end{pmatrix} + D\nabla^2\mathbf{M}, \tag{1.11}$$

where Fick's law is employed to describe the self diffusion of the net magnetization.

About a decade later, in 1965, Stejskal & Tanner designed the *pulsed gradient spin echo* (PGSE) experiment by modifying Hahn's spin echo experiment with two identical magnetic gradients around the 180^o RF pulse to encode the transverse phase of the diffusing spin bearing particles [62, 61] (Fig. 1.4). This made it easier to measure the decay in the transverse signal due to diffusion, and from there the diffusion coefficient. The PGSE experiment established the field of dNMR.

In the PGSE experiment the first gradient $\mathbf{G}$ of duration δ spatially encodes the phase of the individual spins (by dephasing them by an amount dependent on their position), and the effects of this gradient are undone by the second identical gradient after the 180^o RF pulse which flips the spins around (implying an effect $-\mathbf{G}$ from the second gradient). This results in a complete recovery of the signal since the magnitude of transverse magnetization vector $\mathbf{M}_{xy}$ depends on the phase coherence of the individual spins. However, if the individual spins move due to diffusion during the period Δ, between the two pulsed gradients, then the effects of the second gradient isn't the exact opposite of the first gradient ($-\mathbf{G}$) that was used to encode their phases. This leads to a partial phase incoherence – resulting in a reduced transverse magnetization $\mathbf{M}_{xy}$, implying a loss in the spin echo signal. Since the signal decay is related to the rate of diffusion or the diffusion coefficient, measuring the signal decay makes it possible to measure the diffusion coefficient.

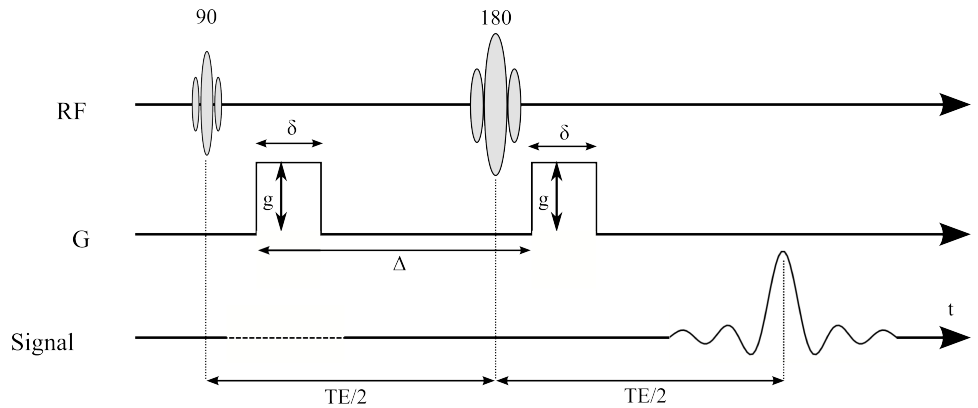

Fig. 1.4 The pulsed gradient spin echo (PGSE) sequence. Two identical gradients are applied around the 180^o RF pulse of Hahn's spin echo experiment. This encodes the transverse phase of the diffusing spin bearing particles. It then becomes easier to measure the decay of the signal due to diffusion.

Stejskal and Tanner provided the mathematical solution to the Bloch-Torrey differential equation for their PGSE experiment, which became the corner stone equation for dNMR as the Stejskal-Tanner equation for the signal:

$$S = S_0 \exp\left(-\gamma^2\delta^2 g^2 \left(\Delta - \frac{\delta}{3}\right) D\right) = S_0 \exp\left(-bD\right), \tag{1.12}$$

where S is the magnitude of the signal decay due to diffusion, S_0 is the magnitude of the signal in the absence of a diffusion encoding gradient, Δ is the time between the two gradients, δ is the application time of each gradient, and $b = \gamma^2\delta^2 g^2 \left(\Delta - \frac{\delta}{3}\right)$ is the b-value. The modifications introduced by Stejskal and Tanner in the PGSE experiment, therefore, makes it possible to measure the diffusion coefficient D a regular spin-echo experiment in NMR.

In the same year, Stejskal further considered diffusion in anisotropic media by employing the anisotropic Fick's law (Eq. 1.5) instead of the isotropic law (Eq. 1.3), in the Bloch-Torrey equation, which introduces the diffusion tensor $\mathbf{D}$ [61]. He was able to derive the modified Stejskal-Tanner equation incorporating the diffusion tensor in anisotropic media [61]:

$$S = S_0 \exp\left(-\gamma^2\delta^2 g^2 \left(\Delta - \frac{\delta}{3}\right) \mathbf{g}^T\mathbf{D}\mathbf{g}\right) = S_0 \exp\left(-b\mathbf{g}^T\mathbf{D}\mathbf{g}\right). \tag{1.13}$$

However, Stejskal in this seminal paper fell short of providing a method for measuring the diffusion tensor from NMR, which could have preempted diffusion tensor imaging by almost three decades. But he did lay the foundations of the q-space formalism with the "pulsed" gradient assumption.

1.3.4 Narrow Gradient Pulse PGSE: q-space Formalism

Diffusion in the PGSE experiment can also be modelled from a probabilistic or random-walk model driven by the thermal kinetic energy of the spin bearing particles. The PGSE experiment (Fig. 1.4) spatially encodes or labels the transverse phase of the spins using the first gradient, which results in a deliberate dephasing of the transverse magnetization. The purpose of the second gradient after the 180^o RF pulse is to undo the effects of the first gradient and rephase the transverse magnetization. However, if the spins diffuse away from their position between the two gradients, then the transverse magnetization isn't entirely rephased after the second gradient, resulting in a loss of the transverse signal. This can be described by using a random-walk approach for the spin bearing particles.

Under the assumption $\delta \ll \Delta$, which is known as the *narrow gradient pulse* (NGP) condition, which implies that the spins are static during the application of the diffusion encoding gradients $\mathbf{G}(t)$, the dephasing accrued by a spin in the initial position $\mathbf{r}_0$ during the first gradient is [44] $\phi_1 = \gamma \int_0^\delta \mathbf{G}(t)\cdot\mathbf{r}_0 dt = \gamma\delta\mathbf{G}\cdot\mathbf{r}_0$, when $\mathbf{G}(t) = \mathbf{G} = g\mathbf{g}$. Similarly the dephasing accrued by the spin, now in the position $\mathbf{r}$ due to diffusion, during the second gradient is $\phi_2 = \gamma \int_\Delta^{\Delta+\delta} \mathbf{G}(t)\cdot\mathbf{r}dt = \gamma\delta\mathbf{G}\cdot\mathbf{r}$. Since the second gradient is applied after the 180^o RF pulse, which flips the spins around, the net phase shift accrued by a spin is $\phi = \phi_2 - \phi_1 = \gamma\delta\mathbf{G}\cdot(\mathbf{r}-\mathbf{r}_0)$. Of course, if the spins hadn't diffused and had remained static during the period Δ (between the gradients), then the net phase shift would have cancelled out. In other words the amount of net phase shift is proportional to the diffused distance $(\mathbf{r}-\mathbf{r}_0)$.

The NGP condition $\delta \ll \Delta$ can also be interpreted in the way Stejskal proposed it $\delta \to 0$, with $\delta\mathbf{G}$ finite. Although in practice the NGP condition can never be achieved, it provides a powerful insight into the process of measuring diffusion from NMR.

The complex signal generated by individual spins with a net phase shift ϕ is $\exp(i\phi) = \exp\left[i\gamma\delta\mathbf{G}\cdot(\mathbf{r}-\mathbf{r}_0)\right]$ [13, 44]. However, the spin echo signal $E(\mathbf{G},\Delta)$ is the averaged net signal from the spin ensemble, or it is the expected value of the complex signal given the probability of spins starting at $\mathbf{r}_0$ and diffusing to $\mathbf{r}$ in the time Δ. This probability is the product of the probabilities $f(\mathbf{r}_0,0)$, of finding a spin initially at $\mathbf{r}_0$, and $P(\mathbf{r}|\mathbf{r}_0,\Delta)$, of a single spin starting at $\mathbf{r}_0$ and diffusing to $\mathbf{r}$ in time Δ. The product $f(\mathbf{r}_0,0)P(\mathbf{r}|\mathbf{r}_0,\Delta)$ introduces the random-walk model for the spin bearing particles diffusing from $\mathbf{r}_0$ to $\mathbf{r}$, and [13]:

$$E(\mathbf{G},\Delta) = \int f(\mathbf{r}_0,0) \int \exp\left[i\gamma\delta\mathbf{G}\cdot(\mathbf{r}-\mathbf{r}_0)\right] P(\mathbf{r}|\mathbf{r}_0,\Delta) d\mathbf{r} d\mathbf{r}_0. \tag{1.14}$$

This indicates that in the absence of diffusion encoding gradients $E(\mathbf{0}, t) = 1$. In practice $E(\mathbf{G}, \Delta)$ is obtained by dividing the echo signal amplitude from a PGSE experiment with diffusion gradients by the echo signal amplitude from a Hahn spin echo experiment without gradients $E(\mathbf{G}, \Delta) = S(\mathbf{G})/S_0$.

This leads to the q-space formalism by defining a reciprocal space q where [13] $\mathbf{q} := \gamma\delta\mathbf{G}/2\pi$. Inserting $\mathbf{q}$ in Eq. (1.14) gives the q-space signal:

$$E(\mathbf{q}, \Delta) = \int f(\mathbf{r}_0, 0) \int \exp\left[i2\pi\mathbf{q} \cdot (\mathbf{r} - \mathbf{r}_0)\right] P(\mathbf{r}|\mathbf{r}_0, \Delta) d\mathbf{r} d\mathbf{r}_0. \tag{1.15}$$

Assuming the transition probability $P(\mathbf{r}|\mathbf{r}_0, \Delta)$ to be translationally invariant or that the movement of a spin is independent of the movements of the other spins and also of its own position and movements in the past – as in a random-walk, implies that $P(\mathbf{r}|\mathbf{r}_0, \Delta) = P(\Delta\mathbf{r}, \Delta)$, which is the diffusion propagator. Also since in a random-walk the movements of all the particles are independent and identical, and since the complex signal and the diffusion propagator for a spin only depend on the spin displacement $\Delta\mathbf{r} = (\mathbf{r} - \mathbf{r}_0)$, it is useful to consider the *ensemble average propagator* (EAP), which describes the average probability of any spin in the ensemble diffusing by $\Delta\mathbf{r}$ during the time Δt [13]:

$$\overline{P}(\Delta\mathbf{r}, \Delta t) = \int P(\Delta\mathbf{r}, \Delta t) f(\mathbf{r}_0, 0) d\mathbf{r}_0. \tag{1.16}$$

Combining Eqs. (1.15 – 1.16) gives the main result of the q-space formalism [13]:

$$E(\mathbf{q}, t) = \int \overline{P}(\Delta\mathbf{r}, t) \exp\left(i2\pi\mathbf{q} \cdot \Delta\mathbf{r}\right) d\Delta\mathbf{r}, \tag{1.17}$$

which establishes an inverse Fourier Transform relationship between the EAP, henceforth denoted $P(\mathbf{r})$, and the normalized echo signal, henceforth denoted $E(\mathbf{q})$.

This Fourier relationship between the ensemble average diffusion propagator and the diffusion NMR signal ushers in the paradigm change that diffusion can be viewed more than just an intrinsic property, but also as a probe of the microstructure of the underlying medium. This becomes apparent when the medium is anisotropic and has a complex microstructure, which is the case in cerebral white matter where numerous fiber bundles criss-cross at a resolution much finer than that of dMRI.

1.4 From Diffusion MRI to Tissue Microstructure

Although Stejskal in Eq. (1.13) formulated the signal for anisotropic diffusion using a *diffusion tensor* (DT), the reason he fell short of providing a method for estimating the DT is perhaps because he was involved with dNMR. In such experiments it was generally possible to re-orient the experimental setup to align the primary anisotropy direction with the laboratory frame, sufficing it to measure the diffusion coefficient in only three directions [34].

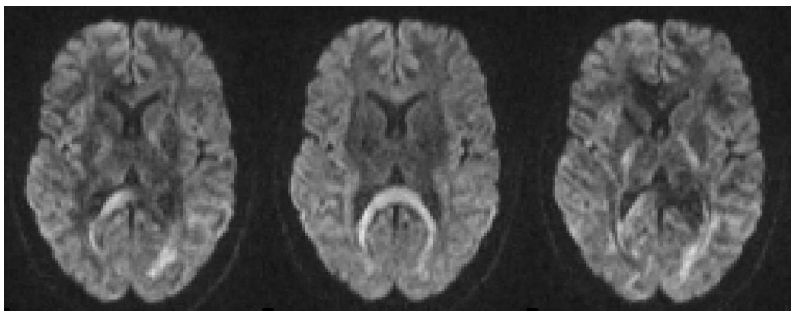

Fig. 1.5 Diffusion Weighted Images of the brain acquired along different gradient encoding directions showing different contrasts.

This however changed with MRI and dMRI, when large anisotropic specimen that couldn't be rotated in the scanner began to be imaged. Imaging such specimen, e.g. cerebral white matter tissue, or the entire brain, revealed that the diffusion coefficient measured in such specimen depended upon the direction of the

diffusion encoding gradient. In other words the dMRI signal decay was different along different gradient directions; or again such dMRI images revealed different contrasts as the diffusion encoding gradient was rotated. These dMRI images were called Diffusion Weighted Images (DWIs). DWIs were at first cryptic because while they revealed the diffusion coefficient, they clearly also indicated that the underlying tissue was highly anisotropic, but they did not provide a method for inferring the preferential directions of this anisotropy. The diffusion coefficients computed from these DWIs using Stejskal-Tanner's isotropic signal decay formulation $S = S_0 \exp(-bD)$ (Eq. 1.12) were called the *apparent diffusion coefficient* (ADC), since these changed in the highly anisotropic tissue depending on the direction of the diffusion encoding gradient (Fig. 1.5). This limitation of the DWI's, and of Stejskal-Tanner's isotropic signal formulation, shifted the interest from measuring only the diffusion coefficient to inferring the preferential diffusion anisotropy directions, or to using diffusion as a probe to infer the tissue's microstructure. This brought forth a whole new meaning to Stejskal's DT formulation, and it's measurement from dMRI, since its diagonalisation provided a local coordinate system that was a good indicator of the preferential diffusion anisotropy directions or the underlying medium's microstructure.

1.4.1 Diffusion Tensor Imaging: The Simplest Model

Diffusion tensor imaging (DTI) was introduced by Basser et al. [5, 6] in 1994, which for the first time provided a method for measuring the DT from dMRI and for inferring the local tissue microstructure from the DT. Starting from Stejskal's equation, Basser et al. defined the **b**-matrix, which also accounted for the imaging gradients in addition to the pure diffusion encoding gradients [5, 6]. They formulated the PGSE echo signal to be:

$$S = S_0 \exp(-tr(\mathbf{bD})), \tag{1.18}$$

where $tr(\mathbf{A})$ represents the trace of the matrix $\mathbf{A}$. This simplifies to Stejskal's formulation (Eq. 1.13) $S = S_0 \exp\left(-b\mathbf{g}^T\mathbf{D}\mathbf{g}\right)$ in the absence of the imaging gradients, or under the consideration that the imaging gradients are small compared to the diffusion encoding gradients, which is mostly true. Otherwise, the **b**-matrix has to be computed from the dynamics of the imaging and the diffusion encoding gradients.

DTI Estimation: $\mathbf{D}$ is a covariance tensor, therefore, it is symmetric and positive definite. This implies that there are six unknowns to be estimated from the DTI signal in Eq. (1.18). Therefore, at least six DWIs, acquired along linearly independent and non-coplanar gradient directions, and a non diffusion weighted or Hahn spin echo (S_0) image is required to measure the six unknown coefficients of $\mathbf{D}$. The linearized version of Eq. (1.18) provides the simplest scheme for doing this [5, 6]:

$$\ln\left(\frac{S}{S_0}\right) = -b_{ij}D_{ij}. \tag{1.19}$$

In practice, often more than six DWIs are used to account for acquisition noise. In the case of N DWIs, the linearized equation for the signal is written in a matrix form:

$$\begin{bmatrix} -\ln(S_1/S_0) \\ -\ln(S_2/S_0) \\ -\ln(S_3/S_0) \\ \vdots \\ -\ln(S_N/S_0) \end{bmatrix} = \begin{bmatrix} b_{11}^1 & 2b_{12}^1 & 2b_{13}^1 & b_{22}^1 & 2b_{23}^1 & b_{33}^1 \\ b_{11}^2 & 2b_{12}^2 & 2b_{13}^2 & b_{22}^2 & 2b_{23}^2 & b_{33}^2 \\ b_{11}^3 & 2b_{12}^3 & 2b_{13}^3 & b_{22}^3 & 2b_{23}^3 & b_{33}^3 \\ \vdots & \vdots & \vdots & \vdots & \vdots & \vdots \\ b_{11}^N & 2b_{12}^N & 2b_{13}^N & b_{22}^N & 2b_{23}^N & b_{33}^N \end{bmatrix} \begin{bmatrix} D_{11} \\ D_{12} \\ D_{13} \\ D_{22} \\ D_{23} \\ D_{33} \end{bmatrix}, \tag{1.20}$$

$$\mathbf{X} = \mathbf{B}\mathbf{d}. \tag{1.21}$$

The easiest option for solving this is to use the least squares optimization $\mathbf{d}_{opt} = argmin_{\mathbf{d}}||\mathbf{X} - \mathbf{B}\mathbf{d}||^2$, which translates to the Moore-Penrose pseudo-inverse solution:

$$\mathbf{d} = (\mathbf{B}^T\mathbf{B})^{-1}\mathbf{B}^T\mathbf{X}.$$

Due to its linear form which only involves matrix manipulations, this solution is extremely rapid. However, it doesn't account for the signal noise or of the distortion to the noise it introduces while taking the logarithms of the signal in the linearization process. Due to DTI's popularity and maturity as a technique of probing tissue microstructures, a number of sophisticated solutions exist for measuring $\mathbf{D}$ from the

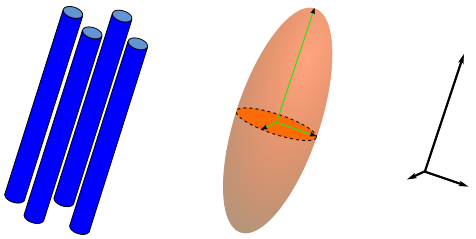

(a) (b) (c)

Fig. 1.6 Microstructure from DTI. Coherent fibers (a) can be inferred from the ellipsoid of the diffusion tensor (DT) (b). The DT also provides a local coordinate system (c) that indicates the preferential diffusion anisotropy directions.

dMRI signal. These range from Basser's original weighted least squares approach [5] which accounts for the logarithmic distortion of the signal noise, to non-linear optimization approaches that account for signal noise, spatial smoothing, and also for constraining the DT to be positive definite [18, 19, 70, 29, 45, 51, 40].

Microstructure from DTI: The consistency between the phenomenological approach and the q-space formalism, under the NGP condition, implies that the propagator describing the diffusion measured by DTI is the Gaussian PDF (Eq. 1.10). This is an oriented Gaussian parameterized by the DT $\mathbf{D}$, or its inverse. The orientation of the PDF can be deduced from the eigen-decomposition of the DT. The eigenvalues and eigenvectors of $\mathbf{D}$ form a local coordinate system that indicates the preferential diffusion direction orienting the Gaussian PDF. In other words it indicates the diffusion direction favoured by the microstructure of the medium. This preferential orientation of the microstructure can be visually represented by the ellipsoid represented by $\mathbf{D}$ whose implicit quadratic form is [6]:

$$\frac{\mathbf{x}^T\mathbf{D}^{-1}\mathbf{x}}{2t} = 1. \tag{1.22}$$

Since $\mathbf{D}$ is symmetric it can be diagonalized $\mathbf{D} = \mathbf{W}^\mathbf{T}\mathbf{\Lambda}\mathbf{W}$, where $\mathbf{W}$ are its orthonormal eigenvectors and $\mathbf{\Lambda}$ is a diagonal matrix whose diagonal elements are its eigenvalues. The canonical form of the diffusion ellipsoid defined by $\mathbf{D}^{-1}$ emerges in the coordinate frame of its eigenvectors:

$$\left(\frac{x'}{\sqrt{2\lambda_1 t}}\right)^2 + \left(\frac{y'}{\sqrt{2\lambda_2 t}}\right)^2 + \left(\frac{z'}{\sqrt{2\lambda_3 t}}\right)^2 = 1.$$

To infer the microstructure of the cerebral white matter from DTI, the fundamental assumption is that the coherent fiber bundle structures formed by the axons hinder the perpendicular diffusion of water molecules (spin bearing ^1H atoms) more than the parallel diffusion. Therefore, the elongation and orientation of the DT are good indicators of these coherent structures or fiber bundles locally. The eigenvector corresponding to the largest eigenvalue, the major eigenvector, indicates the main fiber direction, while the other eigenvectors and eigenvalues indicate diffusion anisotropy in the perpendicular plane (Fig. 1.7).

Scalar Measures: The microstructure of the medium or the white matter can be further characterized from a number of rotationally invariant scalar measures derived from the DT that reveal diffusive properties of the underlying tissue. A number of such scalar measures are of primary importance since they are often used as bio-markers.

- The first is *mean diffusivity* (MD) [4]:
$$\overline{\lambda} = tr(\mathbf{D})/3.$$
- *Fractional anisotropy* (FA) is the other measure which describes the amount of anisotropy presented by the microstructure. It too is derived from the eigenvalues of $\mathbf{D}$ ($\lambda_1 \geq \lambda_2 \geq \lambda_3$) [4]:
$$\mathrm{FA} = \sqrt{\frac{3}{2}}\sqrt{\frac{(\lambda_1-\overline{\lambda})^2 + (\lambda_2-\overline{\lambda})^2 + (\lambda_3-\overline{\lambda})^2}{\lambda_1^2+\lambda_2^2+\lambda_3^2}},$$
- The *Relative anisotropy* (RA) is given by [4]:
$$\mathrm{RA} = \frac{1}{\sqrt{3}}\frac{\sqrt{(\lambda_1-\overline{\lambda})^2 + (\lambda_2-\overline{\lambda})^2 + (\lambda_3-\overline{\lambda})^2}}{\overline{\lambda}}.$$

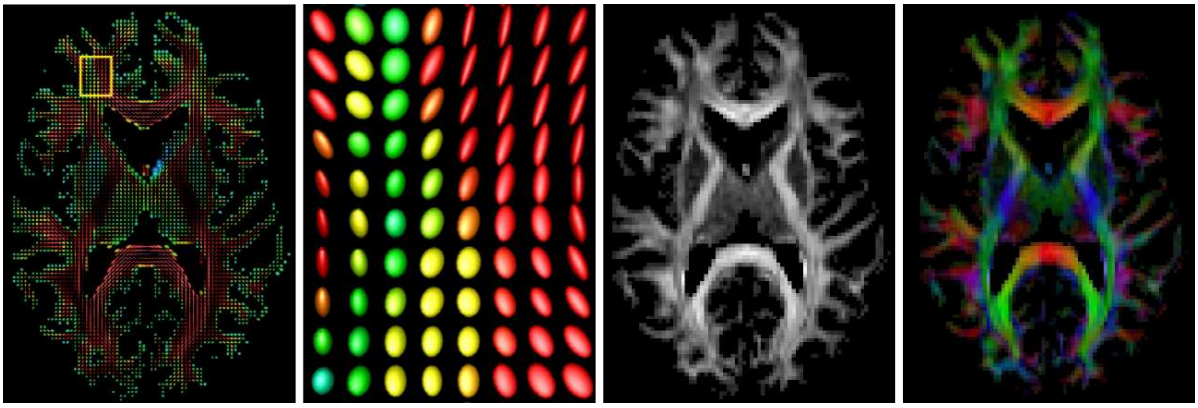

(a) (b) (c) (d)

Fig. 1.7 Diffusion Tensor Imaging (DTI). (a) DTI ellipsoids from an axial slice of the brain. (b) Zoom of highlighted box in (a). (c) Fractional Anisotropy (FA). (d) Colour FA where the colour components RGB represent the unit major eigenvector of the diffusion tensor $\mathbf{e}_1 = [r, g, b]^T$ weighted by FA, or the colours indicate the preferential diffusion anisotropy directions.

- Westin et al. [73] proposed anisotropy measures to discern *linear* c_l, *planar* c_p and *spherical* c_s diffusion tensor shapes:

$$c_l = \frac{\lambda_1 - \lambda_2}{\sqrt{\lambda_1^2 + \lambda_2^2 + \lambda_3^2}}; \quad c_p = \frac{2(\lambda_2 - \lambda_3)}{\sqrt{\lambda_1^2 + \lambda_2^2 + \lambda_3^2}}; \quad c_s = \frac{3\lambda_3}{\sqrt{\lambda_1^2 + \lambda_2^2 + \lambda_3^2}}.$$

1.4.2 Beyond DTI

In DTI, the Gaussian assumption over-simplifies the diffusion of water molecules. While it is adequate for voxels in which there is only a single fiber orientation (or none), it breaks down for voxels in which there are more complex internal structures. This is an important limitation, since the resolution of dMRI acquisitions is between 1mm^3 and 3mm^3 while the physical diameter of fibers can be between 1μm and 30 μm [54, 8]. Research groups currently agree that there is complex fiber architecture in most fiber regions of the brain [53]. In fact, it is currently thought that between one third to two thirds of imaging voxels in the human brain white matter contain multiple fiber bundle crossings [9]. This has led to the development of various High Angular Resolution Diffusion Imaging (HARDI) techniques [69] such as Q-Ball Imaging or Diffusion Spectrum Imaging for exploring the microstructure of biological tissues with greater accuracy.

HARDI samples q-space along as many directions as possible in order to reconstruct estimates of the true diffusion PDF – also referred as the EAP – of water molecules. This true diffusion PDF is model-free and can recover the diffusion of water molecules in any underlying fiber population. HARDI depends on the number of measurements N and the gradient strength (b-value), which directly affects acquisition time and signal to noise ratio in the signal.

1.4.2.1 Diffusion Spectrum Imaging: Recovering the Diffusion EAP

Diffusion spectrum imaging (DSI) introduced by Wedeen et al. [71, 67] in 2000, was the first dMRI method that applied the q-space formalism to measure or estimate the EAP in biological tissue. The forte of the q-space formalism, where diffusion could reveal more than just the intrinsic properties like the diffusion coefficient, and show how it could probe the complex microstructure of the underlying tissue, became quickly apparent. Crossing fiber microstructures were clearly revealed by the geometric forms of the measured EAPs, or their characteristics. Such EAPs clearly represented non-free diffusion and were non-Gaussian. DSI was based on the Fourier Transform relationship between the signal and the EAP described in Eq. (1.17). Although in practice it couldn't satisfy the NGP condition required by the q-space formalism, DSI essentially imaged the q-space densely and reconstructed the EAP via a fast Fourier Transform (FFT). In fact, $\delta \approx \Delta$ in the DSI experiments conducted in [71, 67, 72]. Nonetheless,

the angular results produced by such DSI experiments clearly spoke in favour of q-space imaging – as seen in [58].

DSI, however, considered the modulus Fourier Transform:

$$P(\mathbf{r}) = \int |E(\mathbf{q})| \exp\left(-i2\pi\mathbf{q}\cdot\mathbf{r}\right) d\mathbf{q},$$

in place of the true Fourier Transform, justifying that in the case of pure diffusion the modulus Fourier Transform is equal to the true Fourier Transform. This was done to counter biological motion such as cardiac pulsation, which tended to contaminate the phase of the signal.

Initially visualizing iso-surfaces of the estimated EAP [71], DSI techniques later introduced the *orientation distribution function* (ODF), to emphasize the angular results, which indicated underlying fibers. Two ODFs were used, namely [72] (Fig. 1.8):

$$\Psi_{SA}(\mathbf{u}) = \int_{\mathbf{R}^+} P(r\mathbf{u}) r^2 dr, \quad \mathbf{u} = \mathbf{r}/|\mathbf{r}|, \tag{1.23}$$

and the one introduced by Tuch [67]:

$$\Psi_{T}(\mathbf{u}) = \int_{\mathbf{R}^+} P(r\mathbf{u}) dr, \quad \mathbf{u} = \mathbf{r}/|\mathbf{r}|. \tag{1.24}$$

However, DSI had severe acquisition setbacks. To correctly estimate the EAP, the q-space had to be densely sampled, and also at very high b-values. The DSI sampling scheme was a Cartesian grid inside a sphere in q-space, where both the radius of the sphere – the maximum b-value, and the number of grid-points – the number of acquisitions played important roles in determining the accuracy of the estimated EAP. For example in [71, 72], the maximum b-value was in the range of 20,000 s/mm^2, and the number of acquisitions were more than 500. In comparison, DTI acquisitions are done for b-values of 1000 s/mm^2, and only require a minimum of 6 acquisitions. These demanding requirements played unfavourably for DSI, since its clinical viability was near impossible.

However, DSI was the proof of concept for q-space imaging, which quickly became the popular approach for dMRI, and gave rise to a plethora of techniques for estimating complex EAPs or their characteristics like the ODF. These q-space techniques were developed to overcome the acquisition limitations of DSI.

1.4.2.2 Q-Ball Imaging: Emphasizing the Anisotropic Diffusion Orientation Information

Q-Ball Imaging (QBI) was proposed by Tuch [67, 68] spurred by the facts that DSI had severe acquisition requirements, and that the DSI result of interest wasn't the estimated EAP itself, but rather its radial projection – the ODF, which emphasized angular details. His idea was to retrieve the same angular result with reduced acquisition requirements. His initial attempt was the model based multi-tensor approach which was stricken with instabilities induced by the assumed model. Therefore, he proposed QBI, a

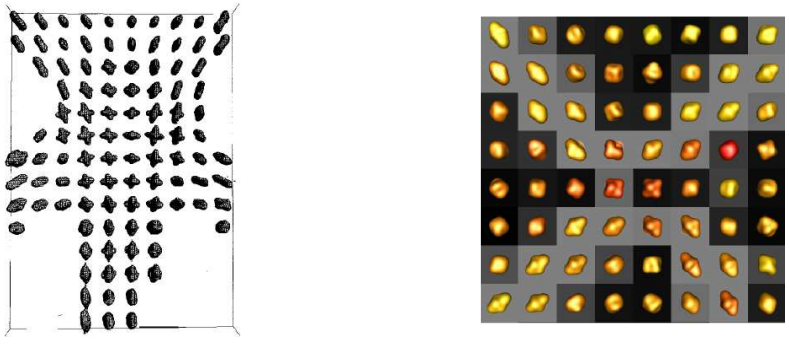

(a) (b)

Fig. 1.8 Diffusion Spectrum Imaging & Q-Ball Imaging. (a) DSI diffusion PDFs from [71]. Corticospinal tract (orientations sup.-inf.) and pontine decussation (left-right). (b) ODFs, estimated from an analytical q-ball approach, such that they represent the angular marginal distributions of the true and unknown EAPs (biological rat phantom).

model free method that sampled q-space only on a sphere or q-shell with fixed q-radius with high angular resolution.

QBI like DSI is based on the q-space formalism and shows promising results, although like DSI, in practice it cannot satisfy the NGP condition [67]. However, QBI became a forerunner to a plethora of q-space methods that attempted to reconstruct the EAP or its characteristics from partial sampling of the q-space. QBI, itself maps spherical acquisitions in q-space to the ODF – a spherical function in real space.

QBI is based on the *Funk Radon transform* (FRT), which is a mapping from a sphere to a sphere $\mathcal{G} : S^2 \rightarrow S^2$. To a point on the sphere, called the pole, the FRT of a spherical function f, assigns the value of the integral of the spherical function along the equator on the plane that has for normal the vector connecting the centre of the sphere to the pole:

$$\mathcal{G}[f(\mathbf{u})](\mathbf{u}) = \int_{S^2} f(\mathbf{u})\delta(\mathbf{u}^T\mathbf{w})d\mathbf{w},$$

where $\mathbf{u}, \mathbf{w} \in S^2$. Using the Fourier slice theorem, Tuch was able to show that the FRT of the signal acquired on a q-sphere was equal to the ODF in Eq. (1.24) blurred by a zeroth-order Bessel function, where the blurring or the width of the Bessel function was inversely proportional to the radius of the acquisition q-sphere.

QBI, therefore, made it possible to reconstruct the angular result of DSI, i.e. the ODF, with fewer acquisitions and without assuming any models. QBI was further boosted by [2, 32, 24], where an analytical solution was proposed, by using the *spherical harmonic* (SH) basis. It was shown that the SHs are the eigenfunctions of the FRT [24]. Letting Y_l^m denote the SH of order l and degree m ($m = -l, \cdots, l$), a modified real and symmetric SH basis is defined. For even order l, a single index j in terms of l and m is used such that $j(l, m) = (l^2 + l + 2)/2 + m$. The modified basis is given by:

$$Y_j = \begin{cases} \sqrt{2}\cdot \mathrm{Re}(Y_l^{|m|}), & \text{if } m < 0 \\ Y_l^m, & \text{if } m = 0 \\ \sqrt{2}\cdot (-1)^{m+1}\cdot \mathrm{Im}(Y_l^m), & \text{if } m > 0 \end{cases}, \tag{1.25}$$

where $\mathrm{Re}(Y_l^m)$ and $\mathrm{Im}(Y_l^m)$ represent the real and imaginary parts of Y_l^m respectively. This modified basis is designed to be real, symmetric and orthonormal, and it is then possible to obtain an analytical estimate of the ODF in Eq. (1.24) with [24]:

$$\Psi_T(\mathbf{u}) = \sum_{j=1}^{L} \underbrace{2\pi P_{l(j)}(0) c_j}_{c'_j} Y_j(\mathbf{u}), \tag{1.26}$$

where $L = (l + 1)(l + 2)/2$ is the number of elements in the modified SH basis, c_j are the SH coefficients describing the input HARDI signal, $P_{l(j)}$ is the Legendre polynomial of order l that is associated with jth element of the modified SH basis and c'_j are the SH coefficients describing the ODF Ψ_T.

Aganj et al. [1] recently proposed an analytical solution to QBI using SHs to compute the ODF in Eq. (1.23), under a mono-exponential assumption of the signal. The ODF in Eq. (1.23) takes into account the solid angle factor during the radial integration, therefore, it is a true marginal density function of the EAP. This solution was also proposed by Vega et al. in [66]. The ODF in Eq. (1.24) proposed by Tuch on the other hand doesn't account for this solid angle, and therefore needs to be numerically normalized after estimation [68] (Fig. 1.8).

1.5 Computational Framework for Processing Diffusion MR Images

Diffusion MRI is a rich source of complex data in the form of images. Processing dMRI data poses a challenging problem since diffusion images can range from scalar images such as DWIs, where each voxel contains a scalar grey-level value, to tensor images such as in DTI, where each voxel contains a 2nd order tensor, to more complex and generic function images such as in DSI or QBI, where each voxel contains a diffusion function such as the EAP in DSI or a spherical function such as the ODF in QBI, represented

as coefficients in a particular basis of choice – such as the SH basis. Therefore, processing such higher dimensional images requires sophisticated mathematical and computational tools.

Processing diffusion images also forms an important part of the dMRI pipeline from acquisition to extraction of meaningful physical and medical information from the data. Operations such as regularization are important for denoising diffusion images as they render the tensor field in DTI or ODF field in QBI more coherent and therefore greatly improve the results of post-processing algorithms such as tractography. A rich body of literature for regularizing tensor fields in DTI can be found in [51, 3, 15, 50, 46]. The capacity to segment tensor images or ODF images makes it possible to identify and reconstruct white matter structures in the brain such as the corpus callosum, which is not possible from simple scalar MR images. However, the extension of such operations from scalar images to tensor fields or ODF fields requires the correct mathematical definitions for spaces of tensors (or EAPs or ODFs) with the appropriate metric. In this section we will present the tools required to process tensor images (DTI), which has seen extensive mathematical development recently. In particular we will present appropriate metrics for the space of symmetric positive definite matrices (or diffusion tensors) $\mathcal{S}ym_n^+$, an estimation algorithm for DTI that ensures that the DT is estimated in $\mathcal{S}ym_n^+$using the Riemannian metric of $\mathcal{S}ym_n^+$ and a segmentation algorithm that uses the Riemannian metric of $\mathcal{S}ym_n^+$to segment regions in a tensor field.

1.5.1 The Affine Invariant Riemannian Metric for Diffusion Tensors

Diffusion tensors are 3×3 symmetric matrices. However, since negative diffusion is non-physical these matrices are also required to be positive definite. In other words DTs belong to the space $\mathcal{S}ym_3^+$ of 3×3 symmetric positive definite matrices, which is a non-Euclidean space. Therefore an appropriate metric needs to be defined on this space which would render it into a Riemannian manifold and which would permit to constrain all operations naturally to $\mathcal{S}ym_3^+$ by using Riemannian geometry. $\mathcal{S}ym_3^+$ naturally inherits the Euclidean and the Frobenius metrics from the space of all matrices, however, $\mathcal{S}ym_3^+$ is neither complete nor closed under these metrics.

A number of works have recently proposed the affine invariant Riemannian metric for $\mathcal{S}ym_n^+$ which has been used extensively to compute on DTs [45, 51, 40]. In [51] the Riemannian metric is derived to be $g_{ij} = g(X,Y) = \langle X,Y\rangle_{\mathbf{S}} = tr\left(\mathbf{S}^{-\frac{1}{2}}X\mathbf{S}^{-1}Y\mathbf{S}^{-\frac{1}{2}}\right), \forall \mathbf{S} \in \mathcal{S}ym_3^+$ and with $X, Y \in T_{\mathbf{S}}\mathcal{S}ym_3^+ = \mathcal{S}ym_3$ the tangent space at $\mathbf{S}$. The geodesic distance between DTs induced by this metric can be computed to be:

$$\mathcal{D}_{Rm}(\mathbf{S}_1, \mathbf{S}_2) = \sqrt{\frac{1}{2}tr\left(\ln^2\left(\mathbf{S}_1^{-1/2}\mathbf{S}_2\mathbf{S}_1^{-1/2}\right)\right)}. \tag{1.27}$$

An equally well known metric for $\mathcal{S}ym_n^+$ is the Log-Euclidean metric [3]. Although it isn't affine invariant and only similarity invariant, computationally it is more efficient than the affine invariant Riemannian metric and resembles closely the latter. The distance between DTs induced by this metric is:

$$\mathcal{D}_{LE}(\mathbf{S}_1, \mathbf{S}_2) = \sqrt{\frac{1}{2}tr\left(\left(\ln(\mathbf{S}_1) - \ln(\mathbf{S}_2)\right)^2\right)}. \tag{1.28}$$

1.5.2 Estimation of DTs in $\mathcal{S}ym_3^+$ Using the Riemannian Metric

Using the appropriate Riemannian metric and geometry for $\mathcal{S}ym_3^+$ can constrain all operations to $\mathcal{S}ym_3^+$. For example using the Riemannian metric for DTI estimation can ensure that the DTs are positive definite or that no negative diffusion will be estimated even in the presence of noisy DWIs. This can be done by using the logarithmically transformed version of the Stejskal-Tanner equation (Eq. 1.13) and considering its explicit least square minimization $E(\mathbf{D}) = \frac{1}{2}\sum_{i=1}^{N}\left(\frac{1}{b}\ln\left(\frac{S_i}{S_0}\right) + \mathbf{g}_i^T\mathbf{D}\mathbf{g}_i\right)^2$. The gradient of this least square functional using the affine invariant Riemannian metric can be shown to be [40]:

$$\nabla E(\mathbf{D}) = \sum_{i=1}^{N}\left(\frac{1}{b}\ln\left(\frac{S_i}{S_0}\right) + \mathbf{g}_i^T\mathbf{D}\mathbf{g}_i\right)\cdot(\mathbf{D}\mathbf{g}_i)(\mathbf{D}\mathbf{g}_i)^T. \tag{1.29}$$

Furthermore the Euclidean gradient descent algorithm required for optimization has to be appropriately replaced by a Riemannian geodesic descent algorithm to respect the Riemannian geometry of $\mathcal{S}ym_3^+$.

1.5.3 Segmentation of a Tensor Field

The goal of segmenting a tensor field or an image of DTs is to compute the optimal 3D surface separating an anatomical structure of interest from the rest of the tensor image (see Fig. 1.9). To do this we follow the method proposed in [23]. The idea will be to treat the tensor field as a field of Gaussian probability density functions and to utilize the affine invariant Riemannian metric on $\mathcal{S}ym_3^+$, which also forms a Riemannian metric in the space of Gaussian density functions, to compute the segmentation boundary. Therefore, a DT at the point x in the image corresponds to the 3D Gaussian distribution $N(x, r)$.

Using the level-set approach and the optimal boundary Γ between the object of interest Ω_1 and the background Ω_2, the level-set $\phi : \Omega_1 \cup \Omega_2 \rightarrow \mathbb{R}$ can be defined as:

$$\begin{cases} \phi(x) = 0, & \text{if} x \in \Gamma \\ \phi(x) = \mathcal{D}_E(x, \Gamma), & \text{if} x \in \Omega_1 \\ \phi(x) = -\mathcal{D}_E(x, \Gamma), & \text{if} x \in \Omega_2 \end{cases} \tag{1.30}$$

where $\mathcal{D}_E(x, \Gamma)$ represents the Euclidean distance between x and Γ. Then according to the geodesic active regions model along with a regularity constraint on the interface, the optimal boundary Γ or the segmentation of the tensor field is obtained by minimizing the functional:

$$E(\phi, P_1, P_2) = \nu \int_{\Omega=\Omega_1 \cup \Omega_2} |\nabla H_\varepsilon(\phi)| dx - \int_\Omega H_\varepsilon(\phi) \ln(P_1(N(x, r))) dx - \int_\Omega (1 - H_\varepsilon(\phi)) \ln(P_2(N(x, r))) dx, \tag{1.31}$$

where $H_\varepsilon(\cdot)$ is a regularized version of the Heaviside function [23], and P_1 and P_2 are the probability distributions of the set of Gaussian distributions $N(x, r)$ in Ω_1 and Ω_2 respectively.

Equation (1.31) can be solved computationally by assuming the distributions P_1 and P_2 themselves to be Gaussians distributions. However, that would require the computation of the mean and the standard deviation of the set of 3D Gaussian distributions $N(x, r)$ constituting Ω_1 and Ω_2. This mean and standard deviation of a set of Gaussian distributions would require a metric to be defined on the space of Gaussian distributions. A number of examples are provided in [23] – the Euclidean metric, the Kullback-Leibler divergence, and the Riemannian metric. We reproduce here only the final example.

Using the affine invariant Riemannian metric on $\mathcal{S}ym_3^+$, which also forms a Riemannian metric on the space of 3D Gaussian distributions $N(x, r)$, it is possible to compute the mean distribution $\overline{N}(X, r)$ of a set of Gaussian distributions by a process of Riemannian geodesic descent – a modified gradi-

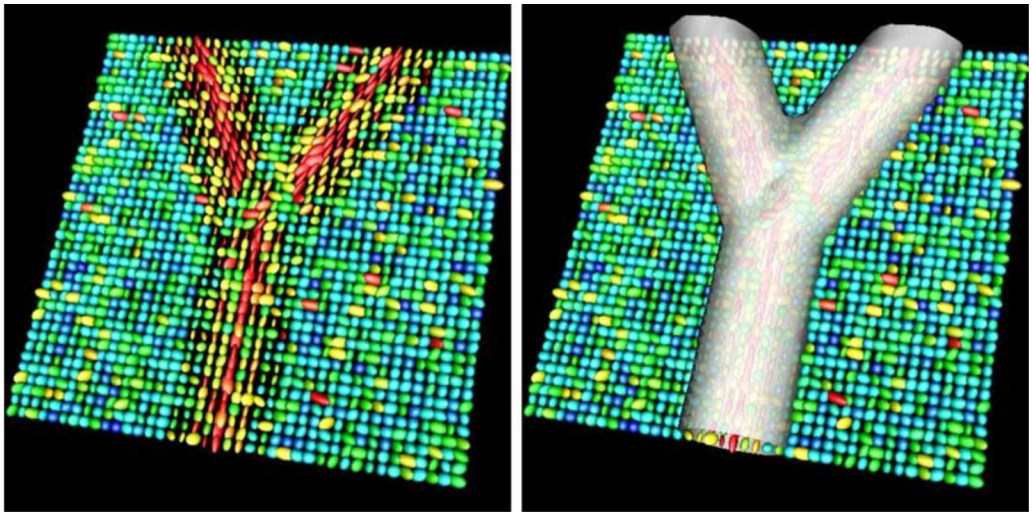

Fig. 1.9 Tensor field segmentation on a synthetic dataset simulating DTI [41].

ent descent process. Similarly the empirical covariance matrix relative to the mean $\overline{N}$ is defined to be $\Lambda_{Rm} = \frac{1}{n-1}\sum_{i=1}^{n}\beta_i\beta_i^T$, with $\beta_i = \overline{N}\ln(N_i^{-1}\overline{N})$ which is the gradient of the squared geodesic distance $\nabla\mathcal{D}^2_{Rm}(N_i,\overline{N})$ in vector form. Using these it is possible to define a generalized Gaussian distribution over the space of 3D Gaussian distributions with a covariance matrix Λ_{Rm} of small variance $\sigma^2 = tr(\Lambda_{Rm})$:

$$P_{Rm}(N \mid \overline{N}, \Lambda_{Rm}) = \frac{1 + O(\sigma^3) + \varepsilon(\sigma/\eta)}{\sqrt{(2\pi)^{m(m+1)/2}|\Lambda_{Rm}|}} \exp\left(\frac{-\beta^T\gamma\beta}{2}\right) \ \forall N \in \mathcal{S}ym_3^+, \tag{1.32}$$

where $\gamma = \Lambda_{Rm}^{-1} - \mathcal{R}/3 + O(\sigma) + \varepsilon(\sigma/\eta)$ with $\mathcal{R}$ as the Ricci curvature tensor at $\overline{N}$, η as the injection radius at $\overline{N}$ and ε such that $\lim_{0^+} x^{-\beta}\varepsilon(x) = 0 \forall \beta \in \mathbb{R}^+$.

1.6 Tractography: Inferring the Connectivity

When DTI/DSI/QBI is performed on the brain, the DT/EAP/ODF – hereafter referred to as the *spherical diffusion function* (SDF), is a local indicator of coherent structures or fiber bundles in the cerebral white matter. However, the process of reconstructing the global structures of fiber bundles by connecting the local information is known as fiber tracing or *tractography*. Tractography graphically reconstructs the connectivity of the cerebral white matter by integrating along the direction indicated by the local geometry of the SDF. It is a modern tool that is unique in the sense that it permits an indirect dissected visualization of the brain in vivo and non-invasively [16]. The underpinnings of tractography are also based on the fundamental assumption of dMRI – the diffusion of water molecules is hindered to a greater extent perpendicular to coherent fiber bundle structures than parallel to these. Therefore, following the geometry of the local diffusion function and integrating along reveals the continuous dominant structure of the fiber bundle. However, in spite of the gain due to its non-invasive nature, tractography can only infer such structures indirectly. Therefore, tractography is acutely sensitive to the local geometry and the error is cumulative. The correct estimation of the local geometry is crucial.

Deterministic tractography is a well established tool that has seen considerable success in researching neurological disorders [20]. Deterministic tractography begins from a seed point and traces along the dominant fiber direction by locally connecting the "fiber" vectors or mathematically becoming tangent to these. Classically the major eigenvector of the diffusion tensor in DTI represented these "fiber" vectors [47, 7, 38]. However, since DTI is ambiguous and cannot accurately describe the fiber directions in regions with complex fiber configurations, DTI tractography, in spite of its successful usage, is known to be prone to errors. Hence the trend in recent years to extend tractography to complex shaped SDFs that describe the underlying fiber directions more accurately [67, 72, 25].

Probabilistic tractography was proposed to address the reliability of deterministic tractography which remains sensitive to a number of parameters. The concept and output of probabilistic tractography is, however, subtly different from determinist tractography. While the latter attempts to find the connectivity between two regions, the former measures the likelihood that two regions are connected, or it provides a connectivity confidence. Given the capabilities and ambiguities of dMRI acquisition and reconstruction schemes of today, due to partial voluming, noise, etc., probabilistic tractography provides a more complete statement. However, probabilistic tractography is also computationally more expensive than deterministic tractography.

1.6.1 Deterministic Tractography

Of the many deterministic tractography algorithms, the continuous *streamline tractography* is a widely used scheme. The continuous version of streamline tractography [7] defined for DTI, considers a fiber tract as a 3D space curve parametrized by its arc-length, $\mathbf{r}(s)$, and describes it by its Frenet equation:

$$\frac{d\mathbf{r}(s)}{ds} = \mathbf{t}(s) = \varepsilon_1(\mathbf{r}(s)), \tag{1.33}$$

where $\mathbf{t}(s)$ the tangent vector to $\mathbf{r}(s)$ at s is equal to the unit major eigenvector $\varepsilon_1(\mathbf{r}(s))$ of the diffusion tensor at $\mathbf{r}(s)$. This implies that fiber tracts are locally tangent to the dominant eigenvector of the

diffusion tensor at every spatial position. The differential equation Eq. (1.33) along with the initial condition $\mathbf{r}(0) = \mathbf{r}_0$ means that starting from $\mathbf{r}_0$, a fiber can be traced by continuously integrating Eq. (1.33) along the direction indicated locally by the major eigenvector of the diffusion tensor at that point.

However, integrating Eq. (1.33) requires two things – first, a spatially continuous tensor (or SDF) field, and second, a numerical integration scheme. In [7], the authors proposed two approaches for estimating a spatially continuous tensor field from a discrete DTI tensor field, namely approximation and interpolation. They also proposed the Euler's method, the 2nd order Runge-Kutta method, and the adaptive 4th order Runge Kutta method as numerical integration schemes. Finally, for stopping they proposed four criteria – the tracts are within the image volume, the tracts are in regions with FA value higher than a threshold, the curvature of a tract is smaller than a threshold, and that a tract is better aligned with the major eigenvector in the next spatial location than any of the two other eigenvectors.

The streamline tractography algorithm can be adapted to SDFs with multiple maxima (EAP/ODF etc.) by modifying Eq. (1.33) to:

$$\frac{d\mathbf{r}(s)}{ds} = \eta_{\theta_{min}}(\mathbf{r}(s)), \quad \mathbf{r}(0) = \eta_{max}(0) \tag{1.34}$$

where $\eta_i(\mathbf{r}(s))$ are all the unit maxima vectors of the SDF at $\mathbf{r}(s)$, η_{max} is the unit maximum vector whose function value is the largest amongst all the η_i, and $\eta_{\theta_{min}}$ is the unit maximum vector in the current step that is most collinear to the unit maximum vector followed by the integration in the previous step. Equation (1.34) and the initial condition state that at the starting point the integrating begins along the dominant maximum direction, and at each consecutive step first all the maxima of the SDF are detected and the maximum direction most collinear to the maximum direction from the previous integration step is chosen to move forward in the integration.

The maximum direction most collinear to the previously chosen maximum direction can be chosen by computing the dot product between the previously chosen maximum direction and all the maxima of the current step, and by considering the absolute values of the dot products. Hence, the maximum chosen for the next integration direction is the maximum whose absolute value of its dot product with the previously chosen maximum direction is the largest. Also to avoid erratic forward and backward steps during the integration, if the value of the dot product is negative, it is necessary to flip the unit maximum direction to point it consistently along the fiber direction, just like in [7].

Since streamline tractography requires a continuous field of SDFs for integrating Eq. (1.34), a continuous field of SDFs can be computed from a simple Euclidean interpolation of the SDFs when the SDFs are expressed in the SH basis. The Euclidean interpolation in the SH basis is equivalent to the L2-norm interpolation of the SDFs, since the SHs form an orthonormal basis [26].

(a) (b)

Fig. 1.10 Deterministic Tractography on ODFs. (a) Three fiber bundles are traced, starting from different seed regions. Red: seeds in the CC (left-right). Blue: seeds in the CST (superio-inferior). Green: seeds in the SLF (anterio-posterior). (b) Zoom into crossing region.

1.6.2 Probabilistic Tractography

General SDF-based (ODF etc.) probabilistic tractography have recently been published in the literature [52, 48, 9, 33, 57, 35, 60, 17] to generalize several existing DT-based methods. First, in [35] parametric spherical deconvolution is used as the SDF [65] and in [9] a mixture of Gaussian model is used to extend the probabilistic Bayesian DT-based tracking [10]. Related to these techniques, [33] uses a Bayesian framework to do global tractography instead of tracking through local orientations. In [52], Monte Carlo particles move inside the continuous field of q-ball diffusion ODF and are subject to a trajectory regularization scheme. In [48], an extension to their DT-based approach [49] is also proposed using a Monte Carlo estimation of the white matter geometry and recently, a Bingham distribution is used to model the peak anisotropy in the fiber distributions [60]. Finally, in [17], large number of M-FACT QBI streamlines are reconstructed and all pathways are reversed-traced from their end points to generate of map of connection probability. In this chapter, a new probabilistic algorithm is presented based on the ODF using a Monte Carlo random walk algorithm.

The new algorithm is an extension of the random walk method proposed in [36] to use the distribution profile of the fiber ODF. It starts off a large number of particles from the same seed point and lets the particles move randomly according to the local ODF estimate, F, and counts the number of times a voxel is reached by the path of a particle. This yields higher transitional probabilities along the main fiber directions. The random walk is stopped when the particle leaves the white matter mask.

For each elementary transition of the particle, the probability for a movement from the seed point x to the target point y in direction $\mathbf{u}_{xy}$ is computed as the product of the local ODFs in direction $\mathbf{u}_{xy}$, i.e.

$$P(x \rightarrow y) = F(\mathbf{u}_{xy})_x \cdot F(\mathbf{u}_{xy})_y \tag{1.35}$$

where $P(x \rightarrow y)$ is the probability for a transition from point x to point y, $F(\mathbf{u}_{xy})_x$ is the ODF at point x in direction xy (by symmetry, direction xy and yx are the same).

The transition directions in the local model are limited to 120 discrete directions corresponding to the angular sampling resolution of the acquired brain data and the step size of the particle step was fixed to 0.5 times the voxel size. A trilinear interpolation of the ODF was used for the subvoxel position and a white matter mask computed from a minimum FA value of 0.1 and a maximum ADC value of 0.0015 was used. A total of 100000 particles were tested for each seed voxel. The connectivity of any given voxel with the seed voxel is estimated by the number of particles that reach the respective voxel, called a *tractogram*.

1.7 Clinical Applications

Diffusion MRI has now proved to be extremely useful for studying the normal and pathological human brain [11, 27] and for improving diagnosis and therapy of brain diseases. It has led to many applications in clinical diagnosis of neurological diseases and disorders, neuroscience applications in assessing connectivity of different brain regions and more recently, therapeutic applications, primarily in neurosurgical planning. Indeed, the sensitivity of diffusion measures to changes in the white matter have led to a wealth of clinical studies using second order diffusion tensor imaging as an in vivo clinical marker and dMRI has opened up a landscape of discoveries for neuroscience and medicine through research and clinical exploration of fiber connectivity and CNS diseases.

The dMRI models and tools presented in this chapter are at the heart of what is strongly needed to better recover, study and understand the anatomical connectivity of the normal and pathological human CNS. These dMRI methodological developments have already been applied in many places to better describe, characterize and quantify abnormalities within the CNS white matter and develop in vivo markers for diseases in clinical neuroscience.

The first and most successful application of dMRI since the early 1990s has been in acute brain ischemia, that emerged from the discovery of Moseley et al. that water diffusion immediately drops after the onset of an ischemic event, when brain cells undergo swelling through cytotoxic edema. This result was later confirmed by different groups using animal models and human patients with stroke.

Since then, many important CNS diseases have attracted the interest of dMRI researchers. Hence, DTI has appeared as a promising tool to look at brain maturation and development, especially to monitor the myelination process, as well as changes in connectivity in relation to functional disorders. Indeed, it

has been shown by many studies that the degree of diffusion anisotropy in white matter increases during the myelination process, so that dMRI could be used to assess brain maturation in children, newborns or premature babies, as well as to characterize white matter disorders in children. DTI has now been used for more than ten years to look, in vivo, at the disorganization of white matter in schizophrenia, which is thought to come from myelin abnormalities. Most neuroimaging studies of schizophrenia have used second order DTI so far, as a means to quantify the integrity of the white matter.

Alzheimer's and Parkinson's diseases, two of the most important neurodegenerative diseases, as well as others like multiple sclerosis have characteristic abnormalities in the microstructure of brain tissues that are not apparent and cannot be revealed reliably by standard imaging techniques. Diffusion MRI can reveal these co-lateral damages to the fibers of the CNS white matter that connect different brain regions.

We in the Athena Project Team, INRIA, France, are currently focusing on the use of ultra high field MRI (3T and 7T) techniques for investigating the structural disorders of the brain stem and of the central deep nuclei in the field of Parkinson's syndrome. This work aims to identify the biomarkers of the pathology by benefitting from the latest developments in the domain of ultra high fields and from the latest image processing innovations in the field of diffusion imaging based on high angular resolution models. Determining the biomarkers for the various forms of Parkinson's disease using high field systems will surely open the way for developing new diagnosis tools at lower field strengths and thus make them available to a clinical environment. Deep brain nuclei are important structures that are involved in a large array of behaviors, such as locomotion, eye-movement, or sleep. Damage to these structures leads to movement disorders such as Parkinson's disease. To date, except for the larger striato-pallidal complex, there are no reliable imaging markers of small deep nuclei. With dMRI and refinements of neuroimaging methods and higher field magnets, imaging of these nuclei has become possible. Together with our collaborators at the Center of Neuroimaging Research (CENIR, Paris, France) and CEA Neurospin (Saclay, France), we are currently conducting a series of experiments in normal volunteers and in patients with basal ganglia pathology to characterize deep brain structures and study the structural disorders of the brainstem in the case of Parkinsonian syndromes. More precisely, we are involved in the data analysis part with the objective to detect the anatomical connectivity of the brainstem structures and their connectivity to the brain and we hope to find new neuroimaging markers of deep brain nuclei that could be used for the diagnosis of Parkinsonian syndromes at an early stage. Possible extension and improvements of the tractography algorithms presented here would be necessary to obtain a satisfactory spatial resolution for identifying the anatomical network involved in Parkinson's disease and improve the characterization of lesions of deep brain structures.

An important application where dMRI is expected to significantly impact in the close future is Traumatic Brain Injury (TBI), which is the damage caused to the brain due to external mechanical force, such as rapid acceleration or deceleration, falls, motor vehicle accidents, impact or penetration by a projectile. The worst injuries can lead to permanent brain damage or death. Because a sudden and violent trauma to the head can cause injury to and shearing of the white matter fibers, it's indeed possible to use dMRI to examine the integrity of white matter that is especially vulnerable to TBI. This opens the way to exciting and challenging problems to quantify and qualify structural changes in white matter.

To this date, a large number of dMRI clinical studies of TBI only uses simple scalar diffusion measurements such as FA and/or MD to characterize the structural abnormalities present along a given fiber pathway to identify pathologies and compare patients with healthy controls. This clearly opens the road to many exciting and challenging problems to examine with more elaborate diffusion models the white matter's integrity and to better quantify and qualify structural changes in white matter.

Through our collaborations with clinical partners and our development of innovative tensor and HARDI processing methods, we are convinced that we can advance further our ability to better understand the architecture of the CNS and help to prove that dMRI can provide a relevant source of useful information, such as in vivo markers of diseases in clinical neuroscience.

Efficient and better tools are therefore more than welcome for undertaking a more systematic study of these abnormalities. For instance, HARDI's improved signal-to-noise ratio can image fiber paths with extraordinary angular detail, identifying more relevant anatomical features, connections and disease biomarkers not seen with conventional MRI.

Moving from quantitative comparisons of scalar values derived from second order diffusion tensors in voxels or along existing pathways, to more relevant measures based on higher order diffusion models and demonstration of qualitative changes in white matter anatomy is extremely challenging.

Therefore, key challenges to tackle include defining new biomarkers related to the quantities, scalar or not, that could be retrieved from High Order Tensors, HARDI, Q-Ball or the EAP to better describe and characterize the biological tissue being analyzed.

Overall, one of the main objectives now is to apply the new methodological developments to improve dMRI as a clinical tool and make it more apt in characterizing and quantifying abnormalities within CNS white matter and to develop better neuroimaging markers for the diagnosis of CNS neurodegenerative diseases. There is a consensus in the neuroimaging field that more elaborate models and HARDI measures will certainly advance research in a large number of CNS diseases.

We are confident that the recent development of novel mathematical analysis tools for dMRI and HARDI will certainly result in fundamental advances for research on stroke, multiple sclerosis, amyotrophic lateral sclerosis, Alzheimer's and Parkinson's diseases, HIV/AIDS, neurosurgery, tumor growth modeling or neuropsychiatric disorders like schizophrenia. Moreover, our understanding of the development of the human brain, the effect of aging or the organization of anatomo-functional networks has already started to greatly benefit from the unprecedented insight that dMRI provides into the brain's microstructure.

1.8 Conclusion

In this chapter we presented an overview of the mathematical tool and framework of dMRI. Diffusion MRI is unique in its capacity at inferring the microstructure of the cerebral white matter in vivo and non-invasively, albeit in an indirect fashion. We first presented a quick perusal of the brain its general structure and organization, the tissues constituting it, and in highlight, its major neuronal pathways interconnecting its various regions. These are central for understanding the diffusion of water molecules in the brain, and for understanding the usefulness of dMRI in studying the brain. The Brownian motion of the water molecules contained in the brain is hindered in the white matter by its fibrous structures in a particular fashion. While the diffusion of water molecules is greatly hindered perpendicular to these structures, the diffusion parallel to these structures is relatively less affected. In other words the diffusing water molecules probe the white matters microstructure. Therefore, since dMRI is sensitive to the diffusion of water molecules, it is used to measure the constrained or anisotropic diffusion of water molecules in the white matter, to infer its major axon fiber bundles non-invasively.

Next we presented the fundamentals of the NMR phenomenon, the diffusion NMR experiment, and reviewed three important diffusion MRI reconstruction algorithms. The NMR experiment can recover several different physical properties from samples which contain spin bearing particles by simply applying a set of magnetic fields and gradients. This forms the core of the non-invasive nature of MRI. However, NMR can only examine a tiny region of a sample or a single spin ensemble and cannot image an entire biological specimen. This is made possible by the spatial encoding technique of MRI, which allows to spatially encode various juxtaposed regions or spin ensembles where NMR can be applied independently. This is done in MRI again using magnetic gradients. Therefore, this allows MRI to examine entire biological specimen, like the brain or the body, in vivo and non-invasively.

One of the properties that NMR can be sensitized to is the Brownian motion of the spin bearing particles in a sample. Therefore, NMR can be used to measure the diffusion properties of a sample by modelling the diffusion of the spin bearing particles in the sample. Since diffusion has been historically modelled in two different ways, namely the Ficks phenomenological laws of diffusion and Einsteins random walk model of Brownian motion, the diffusion NMR signal is also modelled in two ways, namely the Stejskal-Tanner formulation and the q-space formalism.

DTI was the first dMRI technique that was proposed to infer the tissue microstructure. It is the most commonly used technique since its mathematical framework is simple, it has few acquisition requirements and has a number of powerful and practical applications. However, it is limited in regions with microstructural heterogeneity. Many higher order techniques have been therefore proposed recently in dMRI to overcome this limitation of DTI. Of these we presented DSI and QBI, and in particular the ODF.

Diffusion MRI data represents images that contain complex mathematical objects. Recently the computational framework of mathematical tools required to process such images has been vastly improved. We presented the appropriate metrics, in particular the Riemannian metric for $\mathcal{S}ym_n^+$, an estimation algorithm and a segmentation framework using this metric for DTI.

DTI, ODFs and other general SDFs represent the local microstructure of the cerebral white matter in each voxel. As the final mathematical tools we presented tractography algorithms which spatially integrate anisotropy information to reconstruct more global structures such as white matter fiber tracts. Tractography is a unique tool which permits one to indirectly dissect and visualize the brain's white matter in vivo and non-invasively

Finally we concluded the chapter with an overview of major clinical applications to highlight and emphasize the usefulness and strengths of dMRI.

1.9 Online Resources: Softwares and Databases

medINRIA http://www-sop.inria.fr/asclepios/software/MedINRIA/
medINRIA is a multi-platform medical image processing and visualization software, and it's free. Through an intuitive user interface, medINRIA offers from standard to cutting-edge processing functionalities for your medical images such as 2D/3D/4D image visualization, image registration, or dMRI processing and tractography. medINRIA was initially developed by the Asclepios Project Team, INRIA, France. A new version of medINRIA is being jointly developed by the Asclepios, Athena, Parietal and the Visages INRIA Project Teams. It also has a new website at http://med.inria.fr/
Key Features: Log-Euclidean metric, HARDI/ODF, Fiber Tracking.

BrainVISA/Anatomist http://brainvisa.info/
BrainVISA/Anatomist is developed by the Institut Fédératif de Recherche no.49, France.

- BrainVISA is a software, which embodies an image processing factory. A simple control panel allows the user to trigger sequences of treatments on series of images. These treatments are performed by calls to command lines provided by different laboratories. These command lines, hence, are the building blocks on which are built the assembly lines of the factory.
- Anatomist is a visualization software, which main originality is a generic module dedicated to structural data, namely sets of objects linked one another into a graph structure. These objects may be cortical folds inferred from T1 weighted MR data, fiber bundles inferred from MR diffusion weighted data, activated clusters inferred from Statistical Parametric Maps, etc... This module includes a nomenclature control panel, which can drive several brains simultaneously. Anatomist provides also some tools to easily map Statistical Parametric Maps on 3D renderings of the brain, inflated meshes of the cortical surface, etc... Finally, a manual drawing toolbox can be used for various purpose.

Key Features: toolboxes for T1-MRI, dMRI (DTI, QBI), fMRI, MEG/EEG, etc.

FMRIB Software Library (FSL) http://www.fmrib.ox.ac.uk/fsl/index.html
FSL is a comprehensive library of analysis tools for fMRI, MRI and DTI brain imaging data. FSL is written mainly by members of the Analysis Group, fMRIB, Oxford, UK. FSL runs on Apple and PCs (Linux and Windows), and is very easy to install. Most of the tools can be run both from the command line and as GUIs ("point-and-click" graphical user interfaces).
Key Features: Diffusion toolbox contains tools for low-level diffusion parameter reconstruction and probabilistic tractography, including crossing-fiber modelling. It is also capable of tract-based spatial statistics – voxel-wise analysis of multi-subject diffusion data.

Camino Diffusion MRI Toolkit http://web4.cs.ucl.ac.uk/research/medic/camino/pmwiki/pmwiki.php
Camino is a free, open-source, object-oriented software package for analysis and reconstruction of dMRI data, tractography and connectivity mapping. It is developed by the Microstructure Imaging Group, University College London, UK.
Key Features: DTI, multi-tensor model, QBI, MESD/PAS-MRI, deterministic/probabilistic tractography, synthetic data generation and more.

MRI Studio An Image Processing Program https://www.mristudio.org/
MRI Studio is an image processing program running under Windows. It is suitable for such tasks as tensor calculation, color mapping, fiber tracking, and 3D visualization. Most of operations can be done with only a few clicks. DTI Studio is being developed through the support of the Laboratory of Brain

Anatomical MRI and Center for Imaging Science at Johns Hopkins University, USA.
Key Features: DTI, Fiber-tracking and editing, 3D visualization, Region of Interesting (ROI) drawing and statistics, image registration.

3D Slicer http://www.slicer.org/
Slicer, or 3D Slicer, is a free, open source software package for visualization and image analysis. 3D Slicer is natively designed to be available on multiple platforms, including Windows, Linux and Mac Os X. 3D Slicer provides image registration, processing of DTI (diffusion tractography), an interface to external devices for image guidance support, and GPU-enabled volume rendering, among other capabilities. It is developed by the Surgical Planning Laboratory, Brigham and Women's Hospital and the Harvard Medical School, USA.
Key Features: Functionality for segmentation, registration and 3D visualization of multi-modal image data, advanced image analysis algorithms for DTI and fMRI, supports standard image file formats.

MRtrix: MR tractography including crossing fibers http://www.nitrc.org/projects/mrtrix/
MRtrix provides a set of tools to perform diffusion-weighted MRI white matter tractography in the presence of crossing fibers, using Constrained Spherical Deconvolution, and a probabilistic streamlines algorithm. These applications have been written from scratch in C++, using the functionality provided by the GNU Scientific Library, and gtkmm. The software is currently capable of handling DICOM and AnalyseAVW image formats, amongst others. The source code is distributed under the GNU General Public License. MRtrix is being developed by the Brain Research Institute (BRI), Melbourne, Australia.
Key Features: Detection of crossing fibers using Constrained Spherical Deconvolution, probabilistic streamline fiber tracking.

The Fiber Cup Phantom Database http://www.lnao.fr/spip.php?rubrique79
The Fiber Cup was originally intended to be a tractography contest at the MICCAI conference help in London in 2009. Today, the Fiber Cup is still open and is intended to provide a common dataset with known ground truth along with an evaluation methodology to compare and challenge tractography algorithms. It was developed at Neurospin, CEA, France.
Key Features: Provides a MR phantom containing a plethora of crossing, kissing, splitting and bending fiber configurations, acquisitions done at three b-values providing dMRI data on three q-ball shells.

List of Acronyms

ADC Apparent Diffusion Coefficient
CC Corpus Callosum
CNS Central Nervous System
CR Corona Radiata
CST Corticospinal Tract
dMRI Diffusion Magnetic Resonance Imaging
dNMR Diffusion Nuclear Magnetic Resonance
DT Diffusion Tensor
DTI Diffusion Tensor Imaging
DSI Diffusion Spectrum Imaging
DWI Diffusion Weighted Image
EAP Ensemble Average Propagator
EPI Echo Planar Imaging
FA Fractional Anisotropy
FRT Funk Radon Transform
HARDI High Angular Resolution Diffusion Imaging
ILF Inferior Longitudinal Fasciculus
MD Mean Diffusivity
NGP Narrow Gradient Pulse
NMR Nuclear Magnetic Resonance

ODF Orientation Distribution Function
PD Parkinson's disease
PDF Probability Density Function
PGSE Pulsed Gradient Spin Echo
PNS Peripheral Nervous System
QBI Q-Ball Imaging
RA Relative Anisotropy
SDF Spherical Diffusion Function
SH Spherical Harmonics
SLF Superior Longitudinal Fasciculus
TBI Traumatic Brain Injury

References

1. I. Aganj, C. Lenglet, G. Sapiro, E. Yacoub, K. Ugurbil, and N. Harel. Reconstruction of the orientation distribution function in single and multiple shell Q-ball imaging within constant solid angle. *Magnetic Resonance in Medicine*, 64(2):554–566, 2010.
2. A.W. Anderson. Measurements of fiber orientation distributions using high angular resolution diffusion imaging. *Magnetic Resonance in Medicine*, 54:1194–1206, 2005.
3. Vincent Arsigny, Pierre Fillard, Xavier Pennec, and Nicholas Ayache. Log-Euclidean metrics for fast and simple calculus on diffusion tensors. *Magnetic Resonance in Medicine*, 56(2):411–421, August 2006. PMID: 16788917.
4. P. J. Basser. Inferring microstructural features and the physiological state of tissues from diffusion-weighted images. *NMR in Biomedicine*, 8:333–344, 1995.
5. P. J. Basser, J. Mattiello, and D. LeBihan. Estimation of the effective self-diffusion tensor from the NMR spin echo. *Journal of Magnetic Resonance*, B(103):247–254, 1994.
6. P. J. Basser, J. Mattiello, and D. LeBihan. MR diffusion tensor spectroscopy and imaging. *Biophysical Journal*, 66(1):259–267, 1994.
7. P. J. Basser, S. Pajevic, C. Pierpaoli, J. Duda, and A. Aldroubi. In vivo fiber tractography using DT-MRI data. *Magnetic Resonance in Medicine*, 44(4):625–632, October 2000.
8. C. Beaulieu. The basis of anisotropic water diffusion in the nervous system - a technical review. *NMR in Biomedicine*, 15:435–455, 2002.
9. T. E. J. Behrens, H. Johansen-Berg, S. Jbabdi, M. F. S. Rushworth, and M. W. Woolrich. Probabilistic diffusion tractography with multiple fibre orientations. what can we gain? *NeuroImage*, 34(1):144–155, 2007.
10. T.E.J. Behrens, M.W. Woolrich, M. Jenkinson, H. Johansen-Berg, R.G. Nunes, S. Clare, P.M. Matthews, J.M. Brady, and S.M. Smith. Characterization and propagation of uncertainty in Diffusion-Weighted MR Imaging. *Magnetic Resonance in Medicine*, 50:1077–1088, 2003.
11. Denis Le Bihan, Jean-François Mangin, Cyril Poupon, C.A Clark, S. Pappata, N. Molko, and H. Chabriat. Diffusion tensor imaging: concepts and applications. *J Magn Reson Imaging.*, 13(4):534–46, 2001.
12. F. Bloch. Nuclear induction. *Physical Review*, 70:460–474, 1946.
13. P. T. Callaghan. *Principles of nuclear magnetic resonance microscopy*. Oxford University Press, Oxford, 1993.
14. H. Y. Carr and E. M. Purcell. Effects of diffusion on free precession in nuclear magnetic resonance experiments. *Physical Review*, 94:630–638, May 1954.
15. C. A. Castano-Moraga, C. Lenglet, R. Deriche, and J. Ruiz-Alzola. A Riemannian Approach to Anisotropic Filtering of Tensor Fields. *Signal Processing [Special Issue on Tensor Signal Processing]*, 87(2):263–276, 2006.
16. M. Catani, R.J. Howard, S. Pajevic, and D.K. Jones. Virtual in vivo interactive dissection of white matter fasciculi in the human brain. *Neuroimage*, 17:77–94, 2002.
17. Yi P. Chao, Chia Y. Yang, Kuan H. Cho, Chun H. Yeh, Kun H. Chou, Jyh H. Chen, and Ching P. Lin. Probabilistic anatomical connection derived from QBI with MFACT approach. In *2007 Joint Meeting of the 6th International Symposium on Noninavsive Functional Sourse Imaging of the Brain and Heart and the International Conference on Functional Biomedical Imaging*, 2007.
18. C. Chefd'hotel, D. Tschumperlé, R. Deriche, and O. Faugeras. Constrained flows on matrix-valued functions : application to diffusion tensor regularization. In *Proceedings of ECCV'02*, June 2002.
19. C. Chefd'hotel, D. Tschumperlé, R. Deriche, and O. Faugeras. Regularizing flows for constrained matrix-valued images. *J. Math. Imaging Vis.*, 20(1-2):147–162, January 2004.
20. O Ciccarelli, M Catani, H Johansen-Berg, C Clark, and A Thompson. Diffusion-based tractography in neurological disorders: concepts, applications, and future developments. *Lancet Neurol*, 7(8):715–27, 2008.
21. John Crank. *The Mathematics of Diffusion*. Oxford University Press, 2nd edition, 1975.
22. J.J. Dejerine. *Anatomie des Centres Nerveux*. Paris, Rueff & Cie., 1901.
23. Rachid Deriche, David Tschumperlé, Christophe Lenglet, and Mikaël Rousson. Variational Approaches to the Estimation, Regularization and Segmentation of Diffusion Tensor Images. In Chen & Faugeras Paragios, editor, *Mathematical Models of Computer Vision: The Handbook*. Springer, 2005.
24. M. Descoteaux, E. Angelino, S. Fitzgibbons, and R. Deriche. Regularized, Fast, and Robust Analytical Q-Ball Imaging. *Magnetic Resonance in Medicine*, 58:497–510, 2007.
25. M. Descoteaux, R. Deriche, T. R. Knosche, and A. Anwander. Deterministic and Probabilistic Tractography Based on Complex Fibre Orientation Distributions. *IEEE Transactions on Medical Imaging*, 28(2):269–286, 2009.

26. Maxime Descoteaux. *High Angular Resolution Diffusion MRI: From Local Estimation to Segmentation and Tractography*. PhD thesis, Universite de Nice - Sophia Antipolis, February 2008.
27. Q. Dong, R.C. Welsh, T.L. Chenevert, R.C. Carlos, P. Maly-Sundgren, D.M. Gomez-Hassan, and S.K. Mukherji. Clinical applications of diffusion tensor imaging. *Journal of Magnetic Resonance Imaging*, 19:6–18, 2004.
28. A. Einstein. Investigations on the theory of the Brownian movement. *Ann. der Physik*, 1905.
29. P.T. Fletcher and S. Joshi. Principal geodesic analysis on symmetric spaces: Statistics of diffusion tensors. In *Proc. Computer Vision Approaches to Medical Image Analysis*, Prague, May 2004.
30. Henry. Gray. *Gray's Anatomy of the Human Body*. LEA and FEBIGER, 1918, 1918.
31. E.L. Hahn. Spin echoes. *Physical Review*, 80:580–594, 1950.
32. C.P. Hess, P. Mukherjee, E.T. Han, D. Xu, and D.B. Vigneron. Q-ball reconstruction of multimodal fiber orientations using the spherical harmonic basis. *Magnetic Resonance in Medicine*, 56:104–117, 2006.
33. S. Jbabdi, M.W. Woolrich, J.L.R. Andersson, and T.E.J. Behrens. A bayesian framework for global tractography. *NeuroImage*, 37:116–129, 2007.
34. Heidi Johansen-Berg and Timothy E.J. Behrens. *Diffusion MRI, From quantitative measurement to in vivo neuroanatomy*. Elsevier, 1st edition, April 2009.
35. Enrico Kaden, Thomas R. Knosche, and Alfred Anwander. Parametric spherical deconvolution: Inferring anatomical connectivity using diffusion mr imaging. *NeuroImage*, 37:474–488, 2007.
36. M.A. Koch, D.G. Norris, and M. Hund-Georgiadis. An investigation of functional and anatomical connectivity using magnetic resonance imaging. *NeuroImage*, 16:241–250, 2002.
37. P.C. Lauterbur. Image formation by induced local interactions: examples employing nuclear magnetic resonance. *Nature*, 242:190–191, 1973.
38. M. Lazar, D.M. Weinstein, J.S. Tsuruda, K.M. Hasan, K. Arfanakis, M.E. Meyerand, B. Badie, H.A. Rowley, V.Haughton, A. Field, and A.L. Alexander. White matter tractography using diffusion tensor deflection. In *Human Brain Mapping*, volume 18, pages 306–321, 2003.
39. D LeBihan and E. Breton. Imagerie de diffusion *in vivo* par résonnance magnétique nucléaire. *CR Académie des Sciences*, (301):1109–1112, 1985.
40. Christophe Lenglet. *Geometric and Variational Methods for Diffusion Tensor MRI Processing*. PhD thesis, Universite de Nice - Sophia Antipolis, December 2006.
41. Christophe Lenglet, Mickaël Rousson, Rachid Deriche, and Olivier Faugeras. Statistics on the manifold of multivariate normal distributions: Theory and application to diffusion tensor mri processing. *Journal of Mathematical Imaging and Vision*, 25(3):423–444, October 2006.
42. P. Mansfield. Multi-planar image formation using nmr spin echoes. *Journal of Physics C*, 10:55–58, 1977.
43. K.D. Merboldt, W. Hanicke, and J. Frahm. Self-diffusion nmr imaging using stimulated echoes. *J. Magn. Reson.*, 64:479–486, 1985.
44. Ludovico Minati and Władysław P. Węglarz. Physical foundations, models, and methods of diffusion magnetic resonance imaging of the brain: A review. *Concepts in Magnetic Resonance Part A*, 30A(5):278–307, 2007.
45. M. Moakher. A differential geometric approach to the geometric mean of symmetric positive-definite matrices. *SIAM J. Matrix Anal. Appl.*, 26(3):735–747, April 2005.
46. Maher Moakher and Mourad Zéraï. The Riemannian Geometry of the Space of Positive-Definite Matrices and Its Application to the Regularization of Positive-Definite Matrix-Valued Data. *Journal of Mathematical Imaging and Vision*, 40(2):171–187, 2011.
47. S. Mori, B.J. Crain, V.P. Chacko, and P.C.M. Van Zijl. Three-dimensional tracking of axonal projections in the brain by Magnetic Resonance Imaging. *Annals of Neurology*, 45(2):265–269, February 1999.
48. G. J. M. Parker and D. C. Alexander. Probabilistic anatomical connectivity derived from the microscopic persistent angular structure of cerebral tissue. *Philosophical Transactions of the Royal Society, Series B*, 360:893–902, 2005.
49. G.J.M. Parker and D.C Alexander. Probabilistic monte carlo based mapping of cerebral connections utilising whole-brain crossing fibre information. In *IPMI*, pages 684–695, 2003.
50. Ofer Pasternak, Nir Sochen, and Yaniv Assaf. Variational Regularization of Multiple Diffusion Tensor Fields. In Joachim Weickert, Hans Hagen, Gerald Farin, Hans-Christian Hege, David Hoffman, Christopher R. Johnson, and Konrad Polthier, editors, *Visualization and Processing of Tensor Fields*, Mathematics and Visualization, pages 165–176. Springer Berlin Heidelberg, 2006. 10.1007/3-540-31272-2_9.
51. Xavier Pennec, Pierre Fillard, and Nicholas Ayache. A Riemannian Framework for Tensor Computing. *International Journal of Computer Vision*, 66(1):41–66, January 2006. A preliminary version appeared as INRIA Research Report 5255, July 2004.
52. M. Perrin, C. Poupon, Y. Cointepas, B. Rieul, N. Golestani, C. Pallier, D. Riviere, A. Constantinesco, D. Le Bihan, and J.-F. Mangin. Fiber tracking in q-ball fields using regularized particle trajectories. In *Information Processing in Medical Imaging*, pages 52–63, 2005.
53. C. Pierpaoli, P. Jezzard, P.J. Basser, A. Barnett, and G. Di Chiro. Diffusion Tensor MR imaging of human brain. *Radiology*, 201:637–648, 1996.
54. C. Poupon. *Détection des faisceaux de fibres de la substance blanche pour l'étude de la connectivité anatomique cérébrale.* PhD thesis, Ecole Nationale Supérieure des Télécommunications, December 1999.
55. K. Pribam and P. MacLean. Neuronographic analysis of medial and basal cerebral cortex. *J. of Neurophysiology*, 16:324–340, 1953.
56. E.M. Purcell, H.C. Torrey, and R.V. Pound. Resonance absorption by nuclear magnetic moments in a solid. *Physical Review*, 69:37–38, 1946.
57. Peter Savadjiev, Jennifer Campbell, Maxime Descoteaux, Rachid Deriche, G. B. Pike, and K. Siddiqi. Disambiguation of complex subvoxel fibre configurations in high angular resolution fibre tractography. In *Joint Annual Meeting ISMRM-ESMRMB*, Berlin, Germany, 19-25th May 2007, to appear. International Society of Magnetic Resonance in Medicine.
58. Jeremy D. Schmahmann, Deepak N. Pandya, Ruopeng Wang, Guangping Dai, Helen E. D'Arceuil, Alex J. de Crespigny, and Van J. Wedeen. Association fibre pathways of the brain: parallel observations from diffusion spectrum imaging and autoradiography. *Brain*, I30:630–653, 2007.

59. N.R. Selden, D.R. Gitelman, N. Salamon-Murayama, T.B. Parrish, and M.M. Mesulam. Trajectories of cholinergic pathways within the cerebral hemispheres of the human brain. *Brain*, 121:2249–2257, 1998.
60. Kiran K Seunarine, P A Cook, M G Hall, K V Embleton, G J M Parker, and Daniel C Alexander. Exploiting peak anisotropy for tracking through complex structures. *Computer Vision, IEEE International Conference on*, 0:1–8, 2007.
61. E. O. Stejskal. Use of Spin Echoes in a Pulsed Magnetic-Field Gradient to Study Anisotropic, Restricted Diffusion and Flow. *The Journal of Chemical Physics*, 43(10):3597–3603, 1965.
62. E. O. Stejskal and J. E. Tanner. Spin diffusion measurements: Spin echoes in the presence of a time-dependent field gradient. *The Journal of Chemical Physics*, 42(1):288–292, 1965.
63. D.G. Taylor and M.C. Bushell. The spatial mapping of translational diffusion coefficients by the nmr imaging technique. *Phys. Med. Biol.*, 30:345–349, 1985.
64. H. C. Torrey. Bloch equations with diffusion terms. *Phys. Rev.*, 104(3):563–565, November 1956.
65. J. D. Tournier, F. Calamante, D.G. Gadian, and A. Connelly. Direct estimation of the fiber orientation density function from diffusion-weighted MRI data using spherical deconvolution. *NeuroImage*, 23:1176–1185, 2004.
66. Antonio Tristan-Vega, C. F. Westin, and Santiago Aja-Fernandez. A new methodology for the estimation of fiber populations in the white matter of the brain with the Funk-Radon transform. *NeuroImage*, 49:1301–1315, 2010.
67. D. Tuch. *Diffusion MRI of Complex Tissue Structure*. PhD thesis, Harvard University and Massachusetts Institute of Technology, 2002.
68. D. Tuch. Q-ball imaging. *Magnetic Resonance in Medicine*, 52(6):1358–1372, 2004.
69. D.S. Tuch, J.W. Belliveau, T.G. Reese, and V.J. Wedeen. High angular resolution imaging of the human brain. In *Proceedings of the International Society for the Magnetic Resonance in Medecine*, Philadelphia, April 1999.
70. Z. Wang, B. C. Vemuri, Y. Chen, and T. H. Mareci. A constrained variational principle for direct estimation and smoothing of the diffusion tensor field from complex DWI. *IEEE Transactions on Medical Imaging*, 23(8):930–939, 2004.
71. Van J. Wedeen. Mapping fiber orientation spectra in cerebral white matter with Fourier transform diffusion MRI. In *In Proc. of the 8th Annual Meeting of ISMRM*, page 82, 2000.
72. Van J. Wedeen, Patric Hagmann, Wen-Yih Isaac Tseng, Timothy G. Reese, and Robert M. Weisskoff. Mapping complex tissue architecture with diffusion spectrum magnetic resonance imaging. *Magn. Reson. Med.*, 54(6):1377–1386, 2005.
73. C.F. Westin, S.E. Maier, H. Mamata, A. Nabavi, F.A. Jolesz, and R. Kikinis. Processing and Visualization for Diffusion Tensor MRI. *Medical Image Analysis*, 6(2):93–108, June 2002.
74. T. H. Williams, N. Gluhbegovic, and J. Jew. *The human brain: dissections of the real brain*. Virtual Hospital, 1997.
75. M.P. Young, G. Burns, and J.W. Scannell. *The Analysis of Cortical Connectivity*. Landes Bioscience, October 1995.

Index